The Astrophysical Journal Letters, 942:L9 (20pp), 2023 January 1 https://doi.org/10.3847/2041-8213/aca80c

First Batch of $z \approx 11$–20 Candidate Objects Revealed by the James Webb Space Telescope Early Release Observations on SMACS 0723-73

Haojing Yan[1], Zhiyuan Ma[2], Chenxiaoji Ling[1], Cheng Cheng[3], and Jia-Sheng Huang[3]
[1] Department of Physics and Astronomy, University of Missouri-Columbia, Columbia, MO 65211, USA; yanha@missouri.edu
[2] Department of Astronomy, University of Massachusetts, Amherst, MA 01003, USA
[3] Chinese Academy of Sciences South America Center for Astronomy, National Astronomical Observatories, CAS, Beijing 100101, People's Republic of China
Received 2022 August 8; revised 2022 November 4; accepted 2022 November 24; published 2022 December 28

Abstract

On 2022 July 13, NASA released to the whole world the data obtained by the James Webb Space Telescope (JWST) Early Release Observations (ERO). These are the first set of science-grade data from this long-awaited facility, marking the beginning of a new era in astronomy. In the study of the early universe, JWST will allow us to push far beyond $z \approx 11$, the redshift boundary previously imposed by the 1.7 μm red cutoff of the Hubble Space Telescope (HST). In contrast, JWST's NIRCam reaches $\sim$5 μm. Among the JWST ERO targets there is a nearby galaxy cluster SMACS 0723-73, which is a massive cluster and has been long recognized as a potential "cosmic telescope" in amplifying background galaxies. The ERO six-band NIRCam observations on this target have covered an additional flanking field not boosted by gravitational lensing, which also sees far beyond HST. Here we report the result from our search of candidate objects at $z > 11$ using these ERO data. In total, there are 87 such objects identified by using the standard "dropout" technique. These objects are all detected in multiple bands and therefore cannot be spurious. For most of them, their multiband colors are inconsistent with known types of contaminants. If the detected dropout signature is interpreted as the expected Lyman break, it implies that these objects are at $z \approx 11$–20. The large number of such candidate objects at such high redshifts is not expected from the previously favored predictions and demands further investigations. JWST spectroscopy on such objects will be critical.

Unified Astronomy Thesaurus concepts: Galaxy formation (595); Galaxy evolution (594); Early universe (435)

Supporting material: extended figures, machine-readable table

1. Introduction

Over the past decade, the search for high-redshift (high-z) galaxies using deep Hubble Space Telescope (HST) images in fields on both "blank sky" and lensing clusters seems to suggest that the number density of galaxies at $z > 6$ sharply decreases toward higher and higher redshifts (Oesch et al. 2012a, 2012b; Finkelstein et al. 2012; Yan et al. 2012; Zheng et al. 2012; Coe et al. 2013; McLure et al. 2013; Bradley et al. 2014; Bouwens et al. 2015; McLeod et al. 2016; Ishigaki et al. 2018) and even a dearth of galaxies at $z > 10$ (Oesch et al. 2018). This, if true, would create a severe problem for our understanding of the cosmic hydrogen reionization. There has been a consensus that the reionization ended at $z \approx 6.2$ (Fan et al. 2006; Planck Collaboration et al. 2016). There is also a piece of evidence from the detection of 1.420 GHz (21 cm) H I absorption of the cosmic microwave background that the first stars came into being at $z \approx 17.2$ (spanning $z = 13.7$–22.9; Bowman et al. 2018), which is to say that the reionization should begin at the same redshift. While this result is still under debate, an independent line of evidence also points to a similar redshift as the epoch of the first stars. One example is the gravitationally lensed galaxy MACS 1149-JD1 (Zheng et al. 2012), which is at $z = 9.1096$ based on the Atacama Large Millimeter/submillimeter Array (ALMA) detection of its [O III] 88 μm line (Hashimoto et al. 2018). The very existence of oxygen[4] means that the galaxy has already been polluted by the previous generation of stars. To reproduce its spectral energy distribution (SED), especially its Balmer break, these authors found that the onset of the galaxy must be $\sim$290 Myr earlier, i.e., at the formation redshift $z_f \approx 15$. It is therefore conceivable that first stars should be formed at an even earlier time (by a few tens of Myr), and so should the beginning of the reionization. All this, however, is inconsistent with the suggestion that the number of galaxies diminishes at $z > 10$ because this would imply that the reionization could not have happened.

HST cuts off at around 1.7 μm at the red end, which limits the highest possible redshift that it could probe to $z \approx 11$. The task of exploring higher redshifts is now transferred to the James Webb Space Telescope (JWST), which just demonstrated its superb performance through the revelation of its Early Release Observations (ERO) on 2022 July 12 (Pontoppidan et al. 2022). The most relevant ERO observations to high-z studies were the NIRCam imaging on the lensing cluster SMACS 0723-73, which was one of the 41 clusters previously observed by HST in the Reionization Lensing Cluster Survey (RELICS; Coe et al. 2019). This field was observed by the NIRCam instrument (among others) in six bands, and the data were made available worldwide on July 13. These were among the very first set of JWST data suitable for high-z studies. Taking advantage of this opportunity, we report in this Letter our

[4] See also the report of probable detection of carbon and oxygen lines in GN-z11 (Jiang et al. 2021).

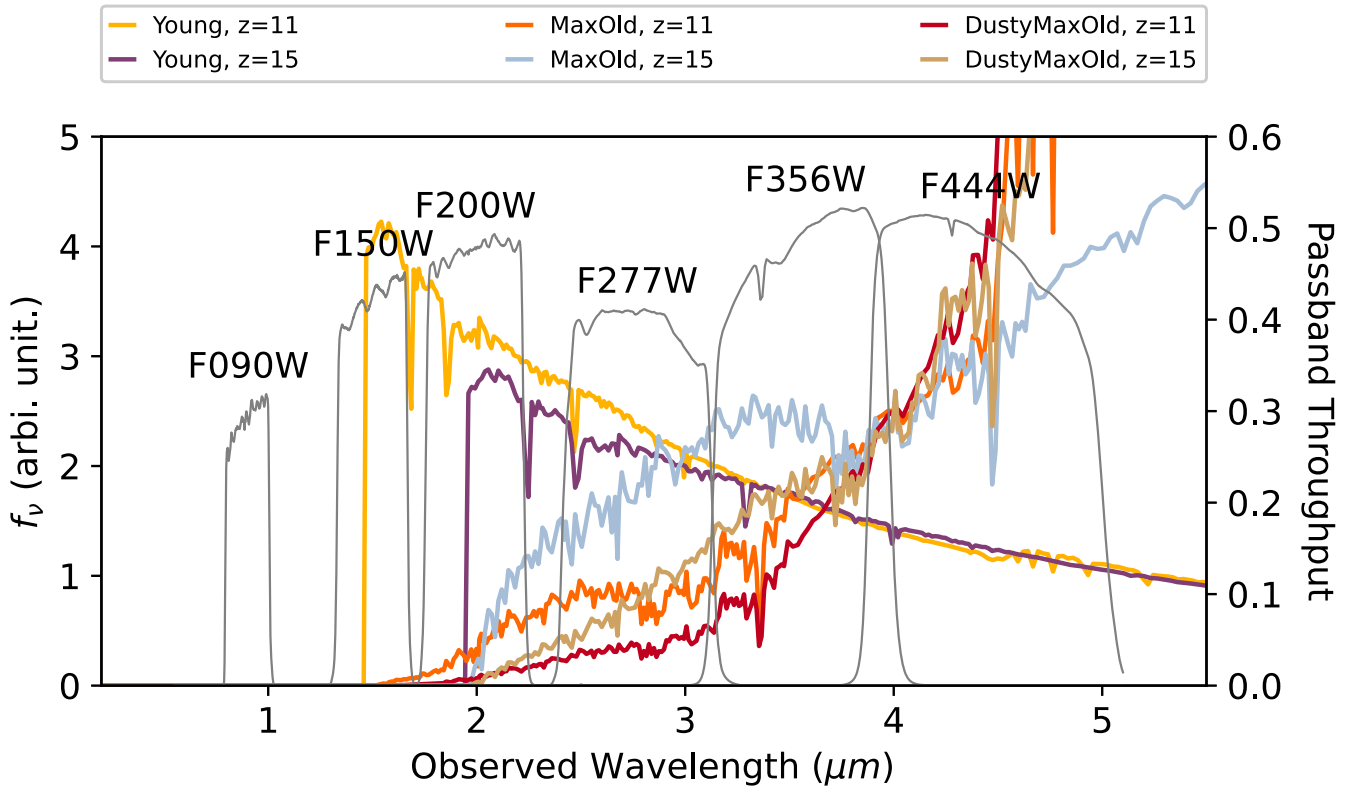

Figure 1. Passbands used in the JWST ERO NIRCam observations on SMACS 0723-73. To demonstrate the dropout technique used for high-z candidate galaxy selection, the spectra of three different model galaxies (as explained in Section 4.1) are superposed. These encompass the bluest and the reddest possibilities. For illustration, they are redshifted to $z = 11$ and $z = 15$.

initial search of $z > 11$ objects in this field, using the now-standard "dropout" technique to identify the characteristic Lyman-break signature in the SEDs of high-z objects (e.g., Steidel et al. 1995; Bouwens et al. 2004; Stanway et al. 2004; Yan & Windhorst 2004). We briefly describe the data and the photometry in Sections 2 and 3, respectively. The selection of $z > 11$ candidate objects is presented in Section 4. We conclude with a discussion of the results in Section 5. All magnitudes quoted are in the AB system. All coordinates are of J2000.0 Equinox. We adopt the following cosmological parameters: $\Omega_M = 0.27$, $\Omega_\Lambda = 0.73$, and $H_0 = 71$ km s^{-1} Mpc^{-1}.

2. JWST ERO NIRCam Data SMACS 0723-73

The NIRCam observations were carried out on UT 2022 June 7 in six bands, namely, F090W, F150W, and F200W in the "short-wavelength" (SW) channel and F277W, F356W, and F444W in the "long wavelength" (LW) channel.[5] As NIRCam operates in these two channels simultaneously on the same fields of view, these SW and LW passbands were observed in pairs. The exposures were obtained using nine `INTRAMODULEBOX` dithers to fill the 4″–5″ gaps in between the SW detectors, which did not fill the 42″–48″ gap between the modules. This resulted in two nonoverlapping fields of $\sim 2\farcm4 \times 2\farcm4$ each in the SW and $\sim 2\farcm2 \times 2\farcm2$ each in the LW. The main part of the cluster was covered by module B in the northeastern direction, while module A observed a flanking field. The dithered positions were determined by the `STANDARD` subpixel dither to optimally sample the point spread functions (PSFs). For each exposure, the `MEDIUM8` readout pattern was adopted in the "up-the-ramp" fitting to determine the count rate. There was one integration per exposure, and each integration contained nine groups. In total, the effective exposure time in each band is 7537.2 seconds. The passband response curves are shown in Figure 1, together with the spectra of three model galaxies redshifted to $z = 11$ and $z = 15$, which we will explain in Section 4.

As it turned out, the fully processed "Stage 3" data made available through the ERO release on July 13 were not suitable for this study due to a number of reasons. Most critically, the astrometric calibrations of different bands have small but notable inconsistencies, which makes photometry difficult. We therefore opted to reprocess these data. We retrieved the products from the Mikulski Archive for Space Telescopes (MAST), which are the calibrated single exposures from the standard JWST data reduction pipeline after the "Level 2b" processing. We then used `calwebb_image3` (version 1.6.1[6]) the "Level 3" pipeline module for imaging data, to combine the single exposures in each band. As the two modules produced two nonoverlapping fields, we processed their data separately. To obtain internally the consistent world coordinate system, we aligned the individual module B images using the RELICS catalog[7] as the reference. For the module A images, we performed the alignment using the first image in F150W as the reference. The pixel scale and the image dimensions were set to

[5] All the JWST data used in this Letter can be found in MAST: doi:10.17909/7rjp-th98.

[6] Three modifications to the pipeline had to be done. The first was to replace `photutil` with `SExtractor` for source detection, the second was to fix a bug in `SkyMatch`, and the third was to allow the use of an external catalog for astrometric calibration.

[7] https://archive.stsci.edu/prepds/relics/#dataaccess

$0\farcs06\,\mathrm{pix}^{-1}$ and 5000×5000 pixels, respectively, in all bands. The internal alignment among the six mosaics is consistent to $\lesssim$0.3 pixel. The absolute astrometric calibration of the final mosaics in both fields were tied to the second data release of Gaia. The astrometry thus determined is accurate to $\sim 0\farcs03$ and $0\farcs09$ (rms) in modules B and A, respectively, in both R.A. and decl. directions. The accuracy in module A is worse because there is no external source catalog comparable to the RELICS catalog used as the intermediate in the calibration.

3. Photometry

The final stacks are in the surface brightness units of $\mathrm{MJy\,sr}^{-1}$. At the scale of $0\farcs06\,\mathrm{pix}^{-1}$, this translates to the magnitude zero-point of 26.581 for all. We derive that the 5σ depths (within $0\farcs2$ radius aperture) in F090W, F150W, F200W, F277W, F356W, and F444W are 28.17, 28.54, 28.73, 29.67, 29.73, and 29.72 (28.16, 28.51, 28.69, 29.49, 29.69, and 29.81) mag, respectively, for module A (module B). The module B images are slightly less sensitive than the ones in module A, presumably due to the impact of the intracluster light (ICL).

We performed matched aperture photometry by running SExtractor (Bertin & Arnouts 1996) in the dual-image mode using the F356W images as the detection images. This choice was made for two reasons. First, the F356W images are about the deepest (see above). Second, the PSF in this band is nearly twice as large as in the SW bands, which makes an aperture defined in this band always sufficient to capture all the source flux in the bluer bands.

We adopted the `MAG_ISO` magnitudes for the color measurements. The sources of our interest are small enough in the images such that the `MAG_ISO` apertures include nearly all the source flux while minimizing the background noise. Hereafter we denote the magnitudes in the six bands as m_{090}, m_{150}, m_{200}, m_{277}, m_{356}, and m_{444}, respectively. We only kept the sources that have $\mathrm{S/N} \geqslant 5.0$ and `ISOAREA_IMAGE` $\geqslant 10$ in F356W.

4. Selecting High-z Candidates as Dropouts

4.1. Selection Overview

Using these data, we searched for candidate high-z objects as F150W, F200W, and F277W dropouts, respectively. If we approximate the throughout curves of the NIRCam bands using rectangles, the *truncation* of a flat spectrum (in f_ν), which is characteristic of a Lyman break at such high redshifts, will create a color decrement of $\sim$0.75 mag in a blue/red pair of bands when the break is redshifted out halfway of the blue band (the "dropout" band). Therefore, we adopted a simple color threshold of 0.8 mag to identify the color decrement caused by the Lyman break, i.e., $m_{150} - m_{200} \geqslant 0.8$, $m_{200} - m_{277} \geqslant 0.8$, and $m_{277} - m_{356} \geqslant 0.8$ mag for the F150W, F200W, and F277W dropouts, respectively. To ensure reliable color measurements, objects must have $\mathrm{S/N} \geqslant 5$ in the red band next to the break (the "drop-in" band), i.e., in F200W, F277W, and F356W for F150W, F200W, and F277W dropouts, respectively.

Of course, the size of the decrement in a real galaxy depends on the actual SED, which can have a wide range of possibilities. This is especially true at such a high redshift, because the age of the universe is short enough that activities of short timescales are not averaged out. This is demonstrated in Figure 1 by the superposed model galaxy spectra that capture the extreme situations. The spectra are generated at $z = 11$ and 15, respectively, using the population synthesis models of Bruzual & Charlot (2003; hereafter BC03). As this is for demonstration purposes, we only consider their solar metallicity models for simplicity. There are three models at each redshift. One is a very young (age of 10 Myr) galaxy with nearly constant star formation, which represents the bluest population that one can get from BC03. We also consider the opposite, a "maximally old template," which is a single burst ("simple stellar population," or SSP) whose age is as old as the age of the universe at the redshift under discussion, i.e., age of 0.5 Gyr (0.3 Gyr) at $z = 11$ ($z = 15$). Such a template has the reddest color among the BC03 models. To make it even redder, we consider the third template, which is a dusty, maximally old template with $A_V = 2.0$ mag and reddened according to the extinction law of Calzetti (2001). As we will show later, our simple color criterion tolerates such a wide range of possibilities reasonably well.

In addition to the 0.8 mag color decrement, we also required that a valid dropout should be a 2σ nondetection in the "veto" band(s), which is (are) the band(s) to the bluer side of the dropout band. After the initial selections were done, we visually inspected the images of all candidates in the six bands to reject contaminators due to various reasons, such as spurious detections around bright objects, image defects, and noise spikes mistakenly included as sources, etc. Due to the nature of photometric error, some of the reported 2σ nondetections in the veto bands are in fact still visible. Such contaminants were also removed in this visual inspection step. The surviving dropouts are all detected in at least two bands, and therefore it is highly unlikely that any of them could be caused by false detections.

If we consider the redshift at which the break moves completely out of the dropout band as the representative redshift of the selection, our F150W, F200W, and F277W dropouts correspond to $z \approx 12.7$ (from 11.3 to 15.4), 17.3 (from 15.4 to 21.8), and 24.7 (from 21.8 to 28.3), respectively. When necessary, we will refer to them collectively as candidate objects at $z \gtrsim 11$. We have 87 of them in total, which are presented in the catalog given in Appendix A.

Dropout selections must consider the possible contamination due to two types of real objects. One type of them are galaxies at lower redshifts dominated by old stellar populations, whose 4000 Å break could be mistaken as a Lyman break. In our case here, 4000 Å break is shifted to F150W, F200W, and F277W at $z \approx 2.7$, 4.0, and 5.9, respectively. To investigate their impact to our color selections, we use a series of BC03 models redshifted to $z = 2.6$–6.0 at the step size of 0.1. These models are SSPs and are maximally old, e.g., with the age of 2.6 Gyr at $z = 2.6$ and 0.9 Gyr at $z = 6.0$. We will refer to them as "mid-z old galaxies." The other type of possible contaminators are Galactic brown dwarfs, whose strong molecular absorption bands could mimic the dropout signature. We use a set of model spectra of Burrows et al. (2006), which cover L and T brown dwarfs with effective temperatures ranging from 2300 to 700 K. As we will show later, the number of possible contaminants caused by either type is very small in our sample.

4.2. SED Analysis

The six-band data afforded us the opportunity to perform SED fitting on our dropouts. The most important quantities derived from this analysis are the photometric redshifts (z_{ph}),

using which we can check whether our dropouts being at high-z can be supported by an independent method. We note that this is fitting the SEDs of dropouts that have already been selected, which is different from selecting high-z candidate galaxies using $z_{\rm ph}$ directly. Dropout selection is based on identifying the Lyman-break signature, which is caused by the Lyman limit and Lyα absorptions due to the intervening H I along the line of sight. Selection based on $z_{\rm ph}$, on the other hand, depends additionally on the galaxy templates in use (i.e., the assumptions on galaxy properties) as well as the fitting method. We also note that getting $z_{\rm ph} > 11$ for a particular dropout should not be taken as a confirmation of its being at high-z. This is because of the statistical nature of $z_{\rm ph}$ and that the template set can never be exhaustive. By the same token, neither should obtaining $z_{\rm ph} < 11$ for a particular dropout be used as a reason to exclude it from the sample. Nevertheless, if we can obtain $z_{\rm ph} > 11$ solutions for the majority of our objects, it will support that they constitute a legitimate sample at $z > 11$.

To this end, we used *Le Phare* (Arnouts et al. 1999; Ilbert et al. 2006) to fit the SEDs of our F150W and F200W dropouts to galaxy templates based on the BC03 models. This allowed us to derive not only $z_{\rm ph}$ but also other physical properties of the galaxies, such as age, stellar mass, star formation rate (SFR), etc. The templates were constructed assuming exponentially declining star formation histories in the form of SFR $\propto e^{-t/\tau}$, where τ ranges from 0 to 13 Gyr (0 for SSP and 13 Gyr to approximate a constant star formation). These models use the Chabrier initial mass function (Chabrier 2003). We adopted the Calzetti extinction law, with $E(B-V)$ ranging from 0 to 1.0 mag. During the fitting, we replaced any $S/N < 2$ detections by the 2σ upper limits in the relevant bands. For the dropouts in module B, we did not correct their SEDs for magnification; such a correction is made when discussing the statistical properties of stellar mass and SFR. Overall, this SED analysis shows that most of our objects are consistent with being at high-z. This is judged from the probability distribution function (PDF) of $z_{\rm ph}$. The full set of Le Phare fitting results are presented in Appendix C. We will discuss this in some detail in the next two sections.

Over the past two decades, there have been discussions on the impact of strong emission lines to broadband photometric diagnostics (e.g., Chary et al. 2005; Cardamone et al. 2009; Atek et al. 2011, 2014; Malkan et al. 2017; Roberts-Borsani et al. 2020). This raises the question whether low-z emission-line objects could mimic high-z dropout colors. We note that this is unlikely when the dropout search employs enough bands. First of all, such a contamination would require multiple strong emission lines to appear in multiple bands to elevate the fluxes to the observed level. The only possible combination of lines are [O II]λ3727, [O III]λ5007, and Hα λ6563 (and some weaker lines in their vicinities), but the lack of a strong, redder line makes it difficult to explain dropouts that are detected in four or more bands. For example, this combination at $z \approx 3.8$–5.0 could elevate the fluxes in F200W, F277W, and F356W to match the brightness of F150W dropouts in these bands; however the brightness in F444W could not be explained. When a dropout is detected in only three bands or less (e.g., an F200W or F277W dropout), such a problem is circumvented; however there are still two other major difficulties that this contamination scheme can hardly overcome. One is the null detections in the veto band(s), which means that such a contaminant would have to be a pure emission-line object without continuum. This implies that the Lyα λ1216 line should also be very strong. For F200W dropouts, the only possible redshift range that the [O II]/[O III]/Hα contamination could occur is $z \approx 5.5$–6.6, but then the Lyα line would show up in F090W and the case would be vetoed. Explaining F277W dropouts in this way has the same difficulty, which leaves $z \approx 7.4$–9.0 as the only range for this contamination scheme because the Lyα line would move to 1.03–1.22 μm that is in between our passbands. However, no such very strong Lyα emitters have been seen at any redshifts. While there are mechanisms to extinguish the Lyα line, it remains an open question whether such mechanisms are applicable to a strong emitter of other lines. The other major difficulty is rareness of strong emission-line objects. To alter the broadband brightness to create the dropout-like color decrements ($\geqslant$0.8 mag), the observed equivalent width (EW) of a line should be $\geqslant$3400 Å to $\geqslant$5150 Å (depending on the band). This translates to rest-frame EW of $\geqslant$500 Å (contaminant at $z \leqslant 5.8$). At $0.35 < z < 2.3$, the HST WFC3 Infrared Spectroscopic Parallel Survey (WISP; Atek et al. 2011) has selected objects with strong [O III] or Hα lines with rest-frame EW $\geqslant$ 200 Å, and the surface density is only about 0.2 arcmin^{-2} for those with rest-frame EW $\geqslant$ 500 Å. Even assuming no redshift evolution, one would get only $\sim$2 such objects within our field. This cannot explain the large number of F200W and F277W dropouts in our sample. Therefore, we believe that low-z emitters are not likely a significant source of contamination to any of our three groups of dropouts. Nevertheless, we still performed SED fitting using templates including emission lines, which were done using EAZY (Brammer et al. 2008). As expected, the majority of our dropouts also have high-z solutions. This set of SED fitting results are also presented in Appendix D. In the rest of the main text, we focus on the SED fitting results using Le Phare with BC03 models.

4.3. F150W Dropouts

The depths of the two bands straddling the Lyman break set the depth of the dropout selection. The nominal 2σ sensitivities (measured within 0.″2 aperture in radius) in F150W are 29.54 and 29.50 mag in modules A and B, respectively. The criterion of $m_{150} - m_{200} \geqslant 0.8$ mag for F150W dropout selection therefore implies that a valid F150W dropout should have $m_{200} \leqslant 28.74$ and 28.70 mag in these two modules, respectively. The subtlety is that the 0.″2 aperture is only an approximation of the real `MAG_ISO` apertures in use. Here we ignore this difference.

There are 32 (28) validated F150W dropouts in module A (B), and the median brightness is $m_{200} = 28.23$ (28.13) mag. There are three and four bright objects with $m_{200} \leqslant 27.5$ mag in modules A and B, respectively.[8] Figure 2 shows the image stamps of an example object in the six NIRCam bands (top), together with its SED fitting results (bottom right; $z_{\rm ph} = 15.0$). Two color–color diagrams are also shown (bottom left and middle) to demonstrate the location of these F150W dropouts in the NIRCam color space. In the $m_{150} - m_{200}$ versus $m_{200} - m_{277}$ projection, which is the main diagnostic diagram for F150W dropouts, all the dropouts (filled red symbols) are

[8] To the first order, the number of the brightest objects from our result is not inconsistent with the recently reported results in other fields observed by JWST during the same period (Naidu et al. 2022; Castellano et al. 2022; Finkelstein et al. 2022).

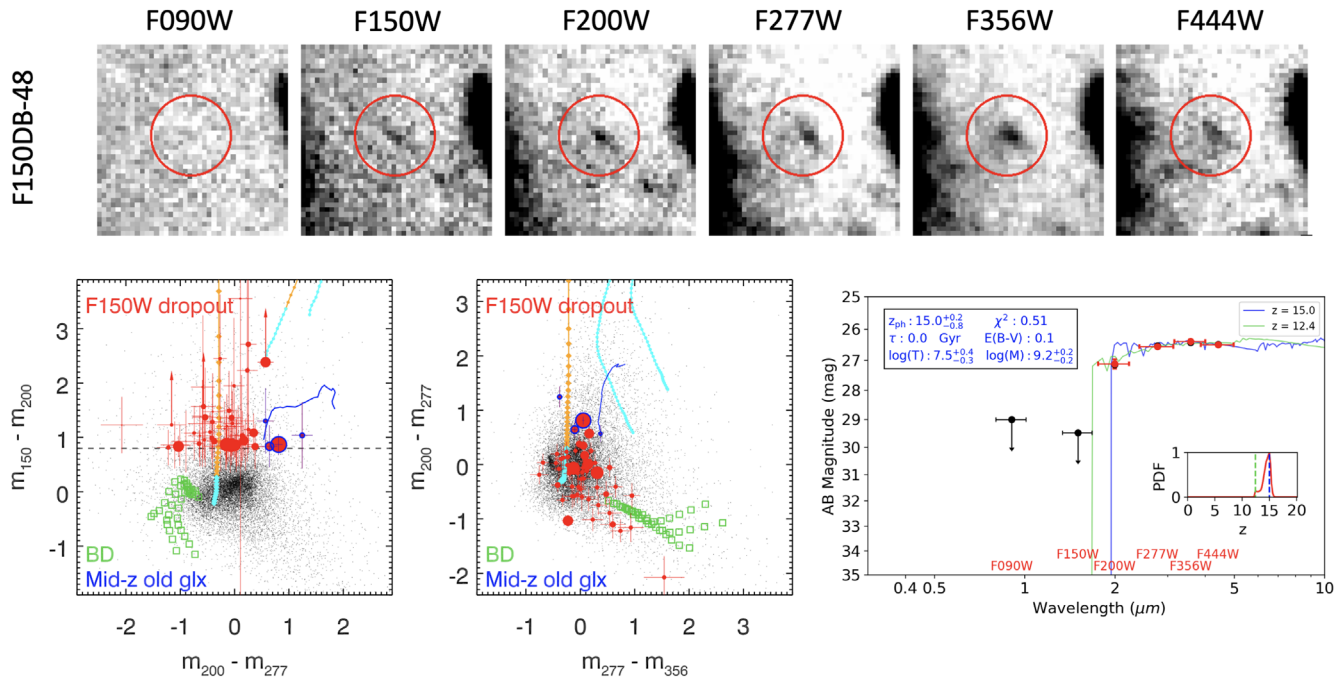

Figure 2. Demonstration of F150W dropouts. The top panel displays the six-band (as labeled) image cutouts ($2\farcs4 \times 2\farcs4$ in size) of such an object selected in module B (its "short ID," or "SID," is labeled to left), whose position is indicated by the red circles ($0\farcs5$ in radius). The SED fitting results of this object are given in the right panel on the bottom row, where the red symbols are the magnitudes and the downward arrow is the upper limit. The lower-right inset shows the PDF, which has two peaks (indicated by the blue and green dashed lines) for this object. The blue and green curves are the best-fit template corresponding to the first and second peaks ($z_{\rm ph} = 15.0$ and 12.4), respectively. Other best-fit parameters corresponding to the first peak are given in the upper-left inset. Two diagnostic color–color diagrams are given in the left and middle panels on the bottom row, which show the positions of all the F150W dropouts in these two projections of the multidimension color space. The filled red circles are the dropouts, while the black dots are the field objects. The dashed horizontal line in the left panel indicates the color threshold of the selection. The color tracks of the three illustrative templates (as in Figure 1) are shown from $z = 10$ to 30 at the step size of 0.2, and different colors (orange or cyan) are used to indicate redshifts above or below $z = 11$. The blue curve indicates the region occupied by mid-z old galaxies. The green open boxes are brown dwarfs. In the left panel, four dropouts (indicated by red circles with a blue outline) seem to be close to the contamination region of mid-z old galaxies. However, in a different projection of the color space as shown in the middle panel, three out of these four are far away from the contamination. In fact, only one dropout (among 60) is indeed in the contamination region in the color space.

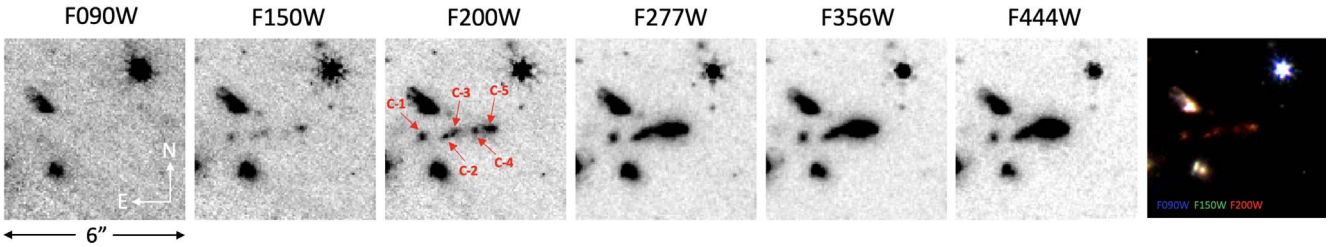

Figure 3. Image stamps of the "chain of five." The passbands are labeled on top. The last panel is a color composite constructed using only the short-wavelength bands to preserve the resolution, where the blue, green, and red colors are F090W, F150W, and F200W, respectively. These five objects are best seen in F200W, where they are labeled. C-1 is isolated, while the other four are severely blended.

far away (>0.5 mag) from the contamination region occupied by brown dwarfs (open green boxes). Four of them (fill red symbols with a blue outline) seem to be close (within 2σ of color errors) to the mid-z old galaxy contamination region (blue curve). However, only one of them is really close to this contamination region in the multidimension color space. This is demonstrated in the $m_{200} - m_{277}$ versus $m_{277} - m_{356}$ projection of the color space, where the other three are seen far away from the contamination. This suggests that the contamination rate is rather low (1 out of 60).

The SED fitting results also support the high-z interpretation of the F150W dropouts; 83% of our objects have the first PDF peak at $z > 10$, and half of the remaining 17% still have the second PDF peak at $z > 10$. Taking these peak $z_{\rm ph}$ as the solutions, the high-z constituents among the F150W dropouts have $z_{\rm ph} = 10.2$–16.0, with the median of $z_{\rm ph} = 11.6$. The sample has median $m_{200} = 28.2$ mag, which corresponds to rest-frame UV absolute magnitude of $M_{\rm UV} = -19.6$ mag.

Among the F150W dropouts, one object in the module B sample is of particular interest.[9] Due to its complexity, we did not include it in the SED analysis. Its image is shown in Figure 3. While its structure in the LW images is not clearly resolved, this object can be discerned as a system of four separate sources. Together with a close neighbor of similar color, the five objects line up a "chain" in the sky, which we dub as "C-1" through "C-5" from east to west. To obtain better photometry, we extracted these sources using the F200W image as the detection image, as it shows all five components

[9] This object is among the "HST H-dark" objects in (Sun et al. 2021, their "ES-025"), which these authors interpreted as high-mass galaxies at $z \approx 3$–5 based on their brightness in the Spitzer IRAC images.

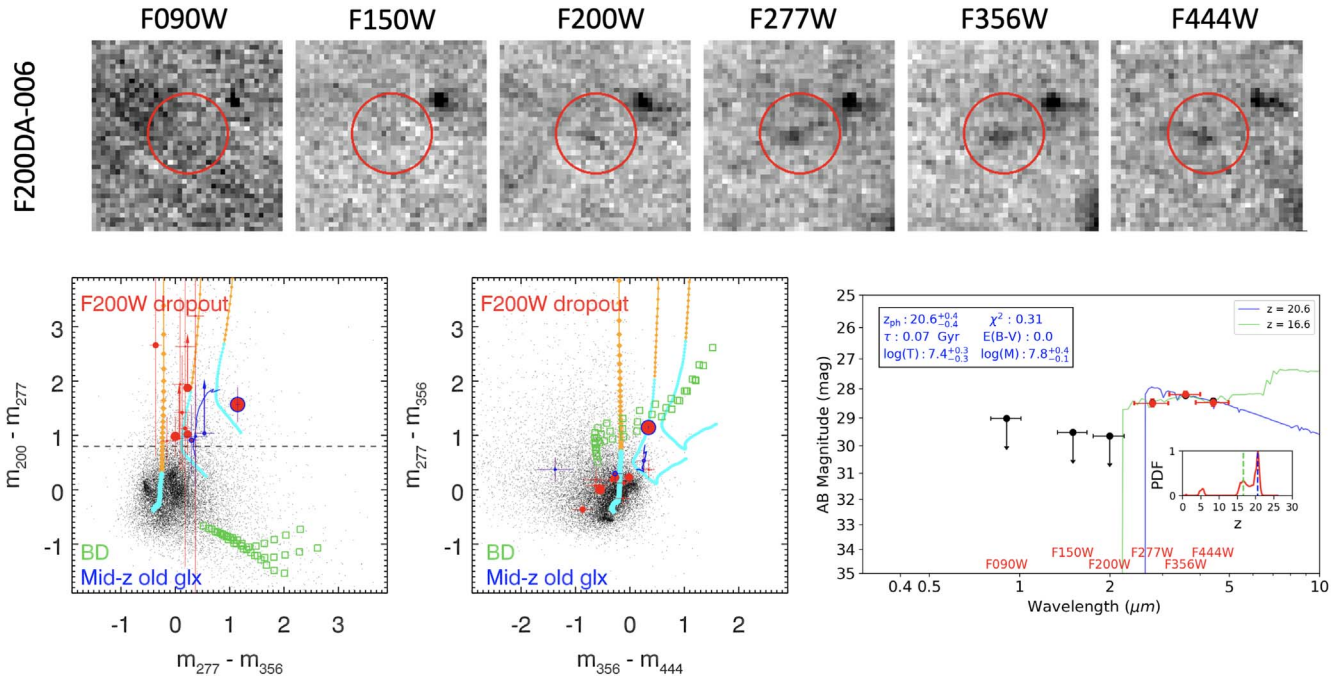

Figure 4. Similar to Figure 2, but for F200W dropouts. The example object is from the sample in module A, and has two PDF peaks corresponding to $z_{\rm ph} = 20.6$ and 16.6, respectively. In the color–color diagrams, the dropout symbol sizes are proportional to their brightness in F277W. In the main diagnostic color–color diagram, there are also four dropouts that seem to be close to the mid-z old galaxy contamination region, but it can be seen from a different projection that most of them actually are not. There is only one F200W dropout (among 15 total) that is indeed close to the contamination region in the color space.

more clearly owing to its better resolution. Despite still suffering from severe blending, this set of photometry suggests that three components, C-2, 3, and 5, are all consistent with being F150W dropouts. C-4 actually qualifies as a F200W dropout. C-1, which is barely visible in F090W, also has a rather red color of $m_{150} - m_{200} = 0.67 \pm 0.08$ suggesting its being at $z \approx 10$. Combining C-2 through C-5 into a single object, it has $m_{356} = 23.1$ mag ($m_{200} = 24.8$ mag), which makes it the brightest system among the high-z candidates in this field. It deserves spectroscopic study in the near future to determine its redshift and to understand the relation between the individual components.

4.4. F200W Dropouts

For F200W dropouts, we consider the 2σ sensitivity limits in F200W, which are 29.73 and 29.69 mag in modules A and B, respectively. Therefore, the brightness threshold for a valid F200W dropout is $m_{277} \leqslant 28.93$ and 28.89 mag in these two modules, respectively. There are 8 (7) validated F200W dropouts in module A (B). An example object is shown in Figure 4, together with its SED fitting results ($z_{\rm ph} = 20.6$). Two diagnostic color–color diagrams are also shown. All these objects are far away from the brown dwarf contamination region. By coincidence, there are also four objects close to the mid-z old galaxy contamination region in the main $m_{200} - m_{277}$ versus $m_{277} - m_{356}$ diagram. However, only one of them is really close to the contamination region, which can be seen in the $m_{277} - m_{356}$ versus $m_{356} - m_{444}$ diagram. Therefore, this suggests that the contamination rate in the F200W dropout sample is also low (1 out of 15).

The SED fitting shows that only one F200W dropout has $z_{\rm ph} < 10$, and the others have $z_{\rm ph}$ ranging from 14.2 to 20.6, with the median of $z_{\rm ph} = 16.0$. The sample has median $m_{277} = 28.6$ mag, which also corresponds to $M_{\rm UV} = -19.6$ mag. There is one bright object from module A that has $m_{277} = 26.85 \pm 0.03$ mag, whose $m_{277} - m_{356}$ color is redder than the reddest mid-z old galaxy but is consistent with being a dusty galaxy at $z > 11$. This is the only one from the module A sample that is brighter than 27.5 mag. Interestingly, no object in the module B sample is brighter than $m_{277} = 27.5$ mag.

4.5. F277W Dropouts

For F277W dropouts, we consider the 2σ sensitivity limits in F277W, which are 30.72 and 30.69 mag in modules A and B, respectively. Therefore, the brightness threshold for a valid F277W dropout is $m_{356} \leqslant 29.86$ and 29.68 mag in these two modules, respectively. There are 10 validated objects in the module A sample but only two in the module B sample. This can be explained by the difference of $\sim$0.2 mag in the brightness thresholds of the two modules. Six out of the 10 module A objects are fainter than $m_{356} = 29.4$ mag, and therefore it is conceivable that severe incompleteness at close to the selection limit in module B significantly reduces the number of detections.

As these dropouts have significant detections in only F356W and F444W, we did not attempt SED fitting. Figure 5 shows the image stamps of one object as an example, together with two color–color diagrams. In the main diagnostic diagram of $m_{277} - m_{356}$ versus $m_{356} - m_{444}$, half of these dropouts are far away from the contamination regions and the other half seem to have similar colors as brown dwarfs. However, these halves are in fact far away from the brown dwarf contamination region in the color space. This can be seen in the $m_{200} - m_{444}$ versus $m_{200} - m_{356}$ projection. If their observed $m_{277} - m_{356}$ color decrements are indeed due to the Lyman break, they are at $z \approx 24.7$. This suggests that the search for "first objects" probably should aim at $z > 20$. Lacking additional information, however, we refrain from further speculating on their nature.

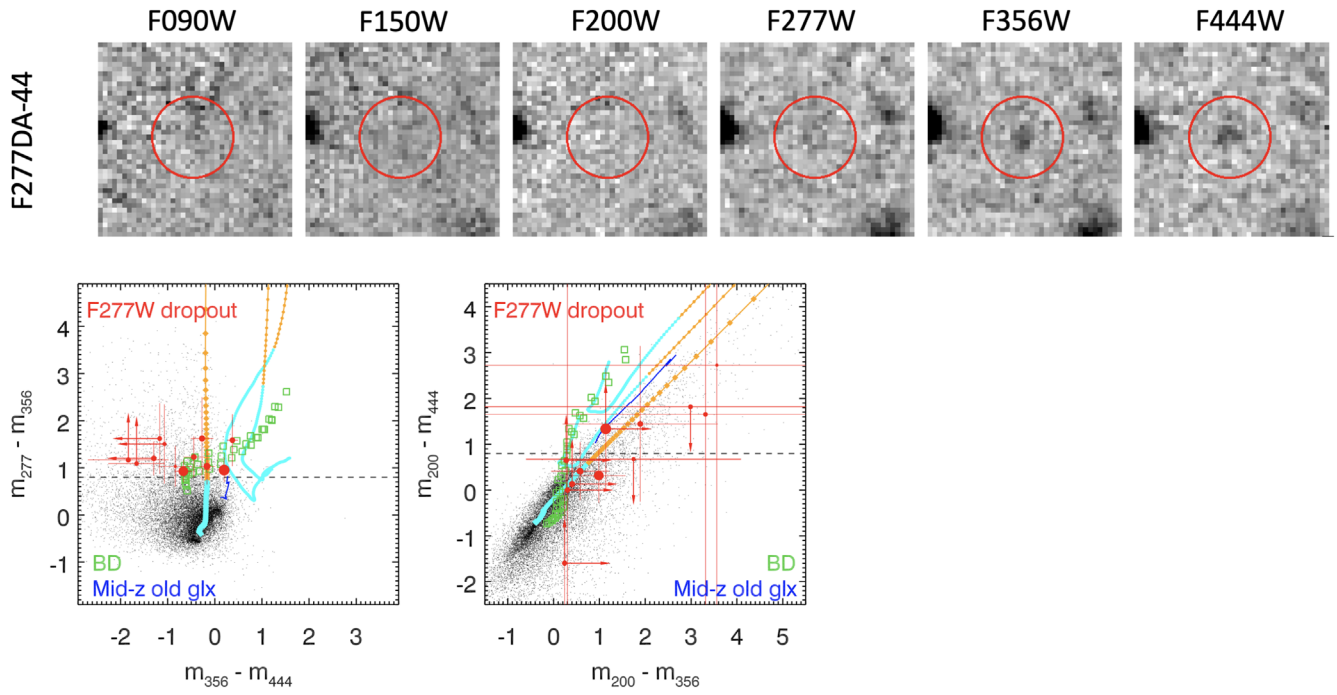

Figure 5. Similar to Figure 2, but for F277W dropouts. The example object is selected in module A. No SED fitting is attempted on these dropouts, as they are only detected in two bands. In the color–color diagrams, their symbol sizes are proportional to their brightness in the F356W band.

5. Discussion

For the dropouts selected in module B, which is on the cluster field, it is necessary to consider the magnification by the cluster. Shortly before the ERO release, a lens model for this cluster was published (Golubchik et al. 2022). This is based on the `Light-Traces-Mass` approach (LTM; Zitrin et al. 2009) and uses the RELICS images and redshifts measured by the Multi Unit Spectroscopic Explorer at the Very Large Telescope. The ERO NIRCam data have revealed new multiply imaged systems, which allow a suite of updated lensing models being built using parametric modeling codes (Caminha et al. 2022; Pascale et al. 2022; Mahler et al. 2022). In this work, we used the LTM model of Golubchik et al. (2022) and the parametric model present in Pascale et al. (2022). The magnification factor (μ) at a given source location is the average of the results from these two models calculated based on $z_{\rm ph}$ as described in Section 4.2.

It is interesting to compare the dropouts selected in the cluster field and the flanking field to see whether and how gravitational lensing plays a role. Overall the cluster field does not produce statistically larger samples; in fact it has slightly fewer dropouts, which is caused by its slightly shallower depths due to the presence of the ICL. Nor does it produce statistically brighter samples. However, it does result in the brightest candidates: two of its F150W dropouts have $m_{200} < 26.5$ mag, one of which is the "chain of five" system. This system has $\mu = 2.3$, while the other has $\mu = 1.6$.

The large number of dropouts presented in this work demands further investigations. For simplicity, we concentrate on the F150W and F200W dropouts in the rest of the discussion. As explained in Section 4, these objects cannot be fake sources because they are all secure detections in more than two bands (some are detected in five bands). In the multidimension color space, the vast majority of these sources (with the exception of one object in each sample) are far away enough from the contamination regions due to mid-z old galaxies and brown dwarfs, and therefore most of them cannot be attributed to contaminations. Recently, Zavala et al. (2022) presented a case where a $z < 6$ dusty starburst mimics the color of an F200W dropout. Their source is detected in millimeter continuum by NOEMA. In contrast, the deep ALMA 1.3 mm mapping in our field, which covers ∼50% of module B, does not reveal any continuum sources at our dropout positions (see Cheng et al. 2022).

On the other hand, the color decrements of our dropouts are consistent with the Lyman break being shifted to $z \gtrsim 11$. If they are indeed at such high redshifts, their large surface densities pose a problem for many predictions. Over the past decade, it has become a dominant view that there is a paucity of galaxies at $z > 10$. Almost all predictions based on theoretical models or extrapolations from the results at lower redshifts expect a rather low surface density of galaxies at $z > 10$ awaiting JWST (see, e.g., Behroozi et al. 2020; Vogelsberger et al. 2020). The only exception is probably the luminosity function proposed by Yan et al. (2010), which would predict ∼94 galaxies at $11.3 \leqslant z \leqslant 15.4$ to be discovered as F150W dropouts over the 11.52 arcmin^2 SMACS 0723-73 NIRCam field to the selection limit of $m_{200} \approx 28.7$ mag as done in this work (but assuming 100% completeness).

Assuming that the F150W and F200W dropouts are indeed at high-z, Figure A1 (see the Appendix) summarizes their properties based on the SED analysis. The top panel shows the $z_{\rm ph}$ distributions of the F150W dropout sample (left) and F200W dropout sample (right). Discarding the interlopers at $z_{\rm ph} < 11$, the median is $z_{\rm ph} = 11.6$ and 15.8 for the F150W and F200W dropouts, respectively, which is largely consistent with the expectation. The middle and the bottom panels show the distributions of three derived quantities for the F150W and F200W dropout samples, respectively. From left to right, these are age (T), stellar mass (M), and SFR. The objects in the cluster field have been demagnified to show the intrinsic M and

SFR. The median ages for both samples are ∼34 Myr, indicating that the formation processes of these galaxies had just begun. The median stellar mass is consistent with this picture, which is 14× and 8.2×10^7 $M_\odot$ for the F150W and F200W dropouts, respectively. They have moderate median SFRs of 19–52 $M_\odot$ yr^{-1}, which means that they could have assembled all their existing stars at such rates over their lifetimes so far.

We note that the surface densities of the F150W and F200W dropouts differ by 4×, increasing from 2.6 arcmin^{-2} for the F200W dropouts to 10.6 arcmin^{-2} for the F150W dropouts. This cannot be due to any selection bias, as the selection of the F200W dropouts in fact has gone ∼0.2 mag deeper (see Section 4.4). If they are at the suggested high redshifts, both samples probe populations of similar luminosity ($M_{\rm UV} \sim -19.6$ mag). The SED analysis results shown in Figure A1 also support that these two samples contain similar objects. Therefore, assuming that most of these dropouts are genuine $z \gtrsim 11$ galaxies, this would suggest a rapid increase of number density over ∼ 140 Myr from $z \approx 17.3$ to $z \approx 12.7$.

We emphasize again that our dropouts are only candidates at $z \gtrsim 11$. Even for those that have good SED fits producing $z_{\rm ph} > 11$, it is still possible that they could be due to some new types of contaminators that we are not familiar with. It is critical to obtain JWST spectroscopy on at least a subset of such candidates so that our future exploration of the high-z universe can be put onto a solid footing.

The authors are grateful to the JWST ERO teams and many behind them for all their hard work that led to the prompt release of the ERO data used in this study. We also thank Adi Zitrin for supplying the lensing magnification calculation. We thank the anonymous referee for the constructive comments and criticisms, which improved the quality of this Letter. H.Y. acknowledges the partial support from the University of Missouri Research Council grant URC-21-005. Z.M. is supported in-part by the National Science Foundation, grant No. 1636621. C.C. is supported by the National Natural Science Foundation of China, No. 11803044, 12173045. This project is based on observations made with the NASA/ESA/CSA James Webb Space Telescope and obtained from the Mikulski Archive for Space Telescopes, which is a collaboration between the Space Telescope Science Institute (STScI/NASA), the Space Telescope European Coordinating Facility (ST-ECF/ESA), and the Canadian Astronomy Data Centre (CADC/NRC/CSA).

Facility: JWST (NIRCam).

Appendix A
Dropout Catalog

The full list of dropouts are presented in Table 1. As stated in Section 4.5, the F277W dropouts are only significantly detected in two to three bands and therefore should be used with caution. Note that the Equatorial coordinates are tied to the DR2 of GAIA, which is different from the astrometric system that the existing RELICS data were calibrated onto. We also note that the "chain of five" system is included in the F150W dropout sample; however only the C-4 component is listed in the catalog as the representative.

Table 1
Catalog of F150W, F200W, and F277 Dropouts

ID	Short ID	m_{090}	m_{150}	m_{200}	m_{277}	m_{356}	m_{444}	μ	$G_{\rm ph}$
F150DB J072314.30-732806.78	F150DB-004	>29.15	>29.50	28.27 ± 0.18	28.28 ± 0.08	28.52 ± 0.08	29.05 ± 0.12	1.92	I
F150DB J072323.97-732758.79	F150DB-007	>29.15	>29.50	28.08 ± 0.18	27.84 ± 0.06	28.10 ± 0.06	28.47 ± 0.07	2.38	I
F150DB J072305.53-732750.69	F150DB-013	>29.15	28.69 ± 0.28	27.76 ± 0.10	28.14 ± 0.08	28.55 ± 0.10	29.47 ± 0.19	2.17	I
F150DB J072312.65-732745.27	F150DB-021	>29.15	28.48 ± 0.34	27.39 ± 0.11	27.04 ± 0.04	26.99 ± 0.03	27.26 ± 0.03	3.09	II
F150DB J072305.73-732743.39	F150DB-023	>29.15	29.57 ± 0.54	28.65 ± 0.19	29.54 ± 0.20	29.00 ± 0.10	30.24 ± 0.29	2.51	IV
F150DB J072323.74-732740.65	F150DB-026	>29.15	29.47 ± 0.54	28.44 ± 0.18	29.08 ± 0.13	28.93 ± 0.10	29.36 ± 0.13	6.38	II
F150DB J072321.44-732736.35	F150DB-031	>29.15	>29.50	28.67 ± 0.21	28.54 ± 0.07	28.85 ± 0.08	28.90 ± 0.08	14.13	II
F150DB J072330.55-732733.12	F150DB-033	>29.15	>29.50	28.22 ± 0.15	27.65 ± 0.04	27.28 ± 0.02	27.47 ± 0.03	4.80	II
F150DB J072311.94-732724.97	F150DB-040	>29.15	27.87 ± 0.18	27.04 ± 0.07	28.07 ± 0.08	28.30 ± 0.08	28.69 ± 0.10	54.94	II
F150DB J072306.63-732725.45	F150DB-041	>29.15	>29.50	28.06 ± 0.19	26.82 ± 0.03	27.20 ± 0.04	27.50 ± 0.05	5.18	I
F150DB J072339.32-732722.31	F150DB-044	>29.15	29.13 ± 0.38	28.23 ± 0.14	28.21 ± 0.06	28.65 ± 0.09	28.81 ± 0.08	2.19	II
F150DB J072301.57-732718.04	F150DB-048	>29.15	>29.50	27.12 ± 0.14	26.55 ± 0.05	26.38 ± 0.03	26.50 ± 0.03	3.24	I
F150DB J072324.58-732715.08	F150DB-050	>29.15	29.22 ± 0.47	28.36 ± 0.18	28.44 ± 0.09	28.84 ± 0.10	29.69 ± 0.21	7.64	II
F150DB J072328.14-732713.89	F150DB-052	>29.15	28.46 ± 0.39	27.63 ± 0.15	27.25 ± 0.05	27.27 ± 0.04	27.81 ± 0.06	16.68	II
F150DB J072312.51-732710.76	F150DB-054	>29.15	29.39 ± 0.39	28.55 ± 0.15	28.96 ± 0.11	28.99 ± 0.09	30.13 ± 0.24	9.09	II
F150DB J072307.27-732710.27	F150DB-056	>29.15	>29.50	28.27 ± 0.15	29.43 ± 0.22	28.50 ± 0.08	28.94 ± 0.11	7.33	II
F150DB J072324.10-732709.84	F150DB-058	>29.15	28.32 ± 0.36	27.48 ± 0.14	26.84 ± 0.04	26.94 ± 0.03	27.05 ± 0.03	10.08	II
F150DB J072304.26-732654.24	F150DB-069	>29.15	>29.50	28.47 ± 0.15	28.87 ± 0.12	29.02 ± 0.11	29.99 ± 0.25	3.10	I
F150DB J072302.23-732641.54	F150DB-075	>29.15	27.46 ± 0.19	26.60 ± 0.08	26.67 ± 0.04	26.79 ± 0.04	27.16 ± 0.05	2.23	I
F150DB J072329.42-732639.79	F150DB-076	>29.15	29.11 ± 0.38	28.26 ± 0.15	28.42 ± 0.08	28.63 ± 0.07	29.42 ± 0.13	2.16	II
F150DB J072313.16-732629.66	F150DB-079	>29.15	>29.50	28.07 ± 0.15	28.17 ± 0.08	28.21 ± 0.07	28.55 ± 0.08	2.11	I
F150DB J072322.76-732625.64	F150DB-082	>29.15	28.76 ± 0.31	27.88 ± 0.11	27.99 ± 0.07	27.88 ± 0.05	28.17 ± 0.06	1.87	II
F150DB J072307.55-732623.82	F150DB-084	>29.15	29.65 ± 0.48	28.49 ± 0.15	28.67 ± 0.08	29.43 ± 0.15	30.51 ± 0.36	1.96	I
F150DB J072314.04-732617.30	F150DB-088	>29.15	29.33 ± 0.27	28.19 ± 0.08	27.94 ± 0.03	28.02 ± 0.03	28.10 ± 0.03	1.77	II
F150DB J072326.24-732613.85	F150DB-090	>29.15	27.14 ± 0.18	26.27 ± 0.07	25.46 ± 0.02	25.41 ± 0.01	25.42 ± 0.01	1.63	II
F150DB J072324.77-732601.30	F150DB-095	>29.15	29.34 ± 0.45	28.47 ± 0.17	28.28 ± 0.07	28.71 ± 0.09	28.84 ± 0.09	1.52	III
F150DB J072325.97-732639.90	F150DB-C_4	>29.15	29.59 ± 0.30	27.65 ± 0.04	25.88 ± 0.00	25.02 ± 0.00	24.36 ± 0.00	2.28	⋯
F200DB J072307.67-732801.58	F200DB-015	>29.15	>29.50	>29.69	28.74 ± 0.12	28.67 ± 0.10	29.31 ± 0.16	1.94	I
F200DB J072322.77-732739.72	F200DB-045	>29.15	>29.50	>29.69	27.82 ± 0.08	27.59 ± 0.05	27.86 ± 0.06	7.86	I
F200DB J072306.42-732719.88	F200DB-086	>29.15	>29.50	28.88 ± 0.37	27.86 ± 0.08	27.63 ± 0.05	27.65 ± 0.05	5.43	II

Table 1
(Continued)

ID	Short ID	m_{090}	m_{150}	m_{200}	m_{277}	m_{356}	m_{444}	μ	$G_{\rm ph}$
F200DB J072337.04-732712.23	F200DB-109	>29.15	>29.50	>29.69	28.88 ± 0.18	28.51 ± 0.12	29.88 ± 0.32	2.54	II
F200DB J072325.35-732646.05	F200DB-159	>29.15	>29.50	>29.69	28.77 ± 0.12	28.68 ± 0.09	29.24 ± 0.14	2.78	I
F200DB J072311.09-732638.03	F200DB-175	>29.15	>29.50	>29.69	28.18 ± 0.07	28.55 ± 0.08	29.42 ± 0.18	2.71	I
F200DB J072312.62-732631.73	F200DB-181	>29.15	>29.50	28.63 ± 0.36	27.65 ± 0.07	27.65 ± 0.06	28.19 ± 0.08	2.20	I
F277DB J072317.55-732825.26	F277DB-001	>29.15	>29.50	>29.69	31.00 ± 0.54	29.41 ± 0.10	29.04 ± 0.07	⋯	⋯
F277DB J072308.41-732622.72	F277DB-013	>29.15	>29.50	>29.69	30.24 ± 0.37	29.21 ± 0.11	29.38 ± 0.13	⋯	⋯
F150DA J072241.01-732955.00	F150DA-005	>29.16	28.88 ± 0.31	28.05 ± 0.12	28.19 ± 0.05	28.36 ± 0.06	28.28 ± 0.06	⋯	I
F150DA J072244.88-732953.69	F150DA-007	>29.16	>29.54	28.38 ± 0.16	28.52 ± 0.07	28.49 ± 0.06	28.64 ± 0.08	⋯	I
F150DA J072252.75-732951.67	F150DA-008	>29.16	>29.54	27.76 ± 0.21	28.30 ± 0.11	27.83 ± 0.07	28.51 ± 0.12	⋯	II
F150DA J072240.09-732946.14	F150DA-010	>29.16	>29.54	28.49 ± 0.21	28.38 ± 0.07	28.73 ± 0.10	28.31 ± 0.07	⋯	I
F150DA J072236.76-732935.68	F150DA-013	>29.16	29.30 ± 0.48	28.22 ± 0.15	28.96 ± 0.12	28.64 ± 0.08	28.77 ± 0.10	⋯	II
F150DA J072244.74-732926.87	F150DA-015	>29.16	29.46 ± 0.53	28.54 ± 0.19	28.51 ± 0.07	28.32 ± 0.06	28.83 ± 0.09	⋯	IV
F150DA J072256.03-732921.94	F150DA-018	>29.16	>29.54	27.97 ± 0.18	28.54 ± 0.14	27.59 ± 0.05	27.93 ± 0.07	⋯	II
F150DA J072239.40-732920.50	F150DA-019	>29.16	29.40 ± 0.47	28.50 ± 0.17	28.65 ± 0.08	28.70 ± 0.09	29.02 ± 0.11	⋯	III
F150DA J072255.88-732917.48	F150DA-020	>29.16	29.32 ± 0.34	28.22 ± 0.10	28.67 ± 0.07	28.66 ± 0.06	28.46 ± 0.06	⋯	I
F150DA J072233.47-732909.57	F150DA-024	>29.16	28.93 ± 0.30	28.12 ± 0.12	29.34 ± 0.17	28.60 ± 0.08	29.02 ± 0.12	⋯	IV
F150DA J072246.02-732908.13	F150DA-026	>29.16	>29.54	28.42 ± 0.18	29.01 ± 0.13	29.16 ± 0.14	28.80 ± 0.10	⋯	I
F150DA J072301.03-732907.20	F150DA-027	>29.16	29.80 ± 0.50	28.57 ± 0.14	30.64 ± 0.36	29.10 ± 0.09	30.31 ± 0.27	⋯	IV
F150DA J072240.65-732900.53	F150DA-031	>29.16	>29.54	28.23 ± 0.15	28.27 ± 0.07	28.16 ± 0.06	28.02 ± 0.05	⋯	I
F150DA J072300.68-732848.43	F150DA-036	>29.16	29.25 ± 0.34	28.30 ± 0.12	28.85 ± 0.10	28.91 ± 0.10	28.82 ± 0.09	⋯	I
F150DA J072302.96-732846.18	F150DA-038	>29.16	>29.54	28.64 ± 0.21	29.24 ± 0.16	29.21 ± 0.15	29.36 ± 0.16	⋯	I
F150DA J072300.58-732847.04	F150DA-039	>29.16	29.00 ± 0.37	28.01 ± 0.13	28.43 ± 0.09	28.13 ± 0.06	28.30 ± 0.08	⋯	II
F150DA J072250.08-732851.05	F150DA-047	>29.16	29.59 ± 0.40	28.73 ± 0.16	29.83 ± 0.21	29.23 ± 0.11	29.84 ± 0.20	⋯	IV
F150DA J072245.00-732836.90	F150DA-050	>29.16	>29.54	27.94 ± 0.14	27.69 ± 0.06	27.49 ± 0.05	27.45 ± 0.05	⋯	I
F150DA J072226.94-732833.82	F150DA-052	>29.16	29.59 ± 0.54	28.56 ± 0.17	28.49 ± 0.09	28.41 ± 0.08	28.53 ± 0.08	⋯	II
F150DA J072232.48-732833.23	F150DA-053	>29.16	>29.54	28.61 ± 0.15	29.19 ± 0.11	29.30 ± 0.12	29.43 ± 0.13	⋯	I
F150DA J072238.89-732830.88	F150DA-054	>29.16	29.52 ± 0.48	28.64 ± 0.18	28.89 ± 0.09	28.83 ± 0.08	29.19 ± 0.11	⋯	III
F150DA J072258.72-732828.40	F150DA-057	>29.16	27.80 ± 0.20	26.94 ± 0.08	26.93 ± 0.03	26.79 ± 0.03	27.09 ± 0.03	⋯	II
F150DA J072248.28-732827.38	F150DA-058	>29.16	>29.54	27.87 ± 0.15	27.92 ± 0.09	27.38 ± 0.05	27.57 ± 0.06	⋯	I
F150DA J072240.76-732823.77	F150DA-060	>29.16	29.59 ± 0.44	28.64 ± 0.16	28.69 ± 0.08	28.64 ± 0.07	28.75 ± 0.08	⋯	I
F150DA J072254.23-732823.59	F150DA-062	>29.16	28.97 ± 0.44	27.94 ± 0.14	27.80 ± 0.04	28.03 ± 0.05	27.72 ± 0.04	⋯	I
F150DA J072253.83-732823.24	F150DA-063	>29.16	27.50 ± 0.26	26.63 ± 0.10	26.78 ± 0.04	26.47 ± 0.03	26.54 ± 0.03	⋯	II
F150DA J072239.62-732812.19	F150DA-066	>29.16	28.94 ± 0.23	28.06 ± 0.09	28.71 ± 0.07	29.04 ± 0.09	29.05 ± 0.09	⋯	II
F150DA J072238.35-732757.11	F150DA-075	>29.16	>29.54	28.08 ± 0.16	28.49 ± 0.11	27.84 ± 0.06	27.88 ± 0.06	⋯	II
F150DA J072252.23-732755.40	F150DA-077	>29.16	>29.54	28.23 ± 0.10	28.50 ± 0.07	28.48 ± 0.06	28.58 ± 0.07	⋯	I
F150DA J072249.25-732749.89	F150DA-078	>29.16	28.87 ± 0.37	28.01 ± 0.14	27.98 ± 0.06	27.71 ± 0.04	28.15 ± 0.07	⋯	II
F150DA J072249.24-732744.55	F150DA-081	>29.16	>29.54	28.48 ± 0.16	28.49 ± 0.07	28.35 ± 0.06	28.44 ± 0.06	⋯	I
F150DA J072252.78-732741.93	F150DA-082	>29.16	29.11 ± 0.35	28.25 ± 0.14	29.26 ± 0.16	29.04 ± 0.12	28.99 ± 0.11	⋯	III
F150DA J072242.72-732732.31	F150DA-083	>29.16	28.21 ± 0.28	27.27 ± 0.10	27.10 ± 0.04	27.02 ± 0.04	27.54 ± 0.06	⋯	II
F200DA J072240.35-733010.35	F200DA-006	>29.16	>29.54	>29.73	28.48 ± 0.11	28.19 ± 0.08	28.46 ± 0.11	⋯	I
F200DA J072243.92-732915.78	F200DA-033	>29.16	>29.54	28.42 ± 0.32	26.85 ± 0.03	25.70 ± 0.01	25.36 ± 0.01	⋯	IV
F200DA J072305.21-732913.40	F200DA-034	>29.16	>29.54	>29.73	28.85 ± 0.15	28.66 ± 0.11	29.28 ± 0.21	⋯	II
F200DA J072303.93-732906.15	F200DA-040	>29.16	>29.54	>29.73	28.61 ± 0.12	28.48 ± 0.10	28.59 ± 0.11	⋯	I
F200DA J072237.03-732841.58	F200DA-056	>29.16	>29.54	29.71 ± 0.43	28.81 ± 0.08	28.97 ± 0.09	29.09 ± 0.10	⋯	II
F200DA J072231.70-732838.66	F200DA-061	>29.16	>29.54	29.65 ± 0.49	28.52 ± 0.08	28.34 ± 0.06	28.68 ± 0.08	⋯	III
F200DA J072232.43-732806.80	F200DA-089	>29.16	>29.54	>29.73	28.81 ± 0.13	28.44 ± 0.09	28.09 ± 0.06	⋯	I
F200DA J072234.80-732800.23	F200DA-098	>29.16	>29.54	>29.73	28.69 ± 0.16	28.16 ± 0.09	27.90 ± 0.07	⋯	I
F277DA J072247.81-733004.68	F277DA-001	>29.16	>29.54	>29.73	>30.66	29.49 ± 0.15	>30.72	⋯	⋯
F277DA J072225.29-732854.54	F277DA-025	>29.16	>29.54	>29.73	>30.66	29.55 ± 0.16	>30.72	⋯	⋯
F277DA J072241.25-732842.96	F277DA-028	>29.16	>29.54	>29.73	30.62 ± 0.42	29.39 ± 0.12	29.84 ± 0.18	⋯	⋯
F277DA J072300.29-732830.55	F277DA-033	>29.16	>29.54	>29.73	>30.66	29.65 ± 0.18	>30.72	⋯	⋯
F277DA J072235.39-732821.47	F277DA-040	>29.16	>29.54	>29.73	30.84 ± 0.41	29.81 ± 0.15	30.65 ± 0.32	⋯	⋯
F277DA J072256.53-732811.17	F277DA-044	>29.16	>29.54	>29.73	29.55 ± 0.24	28.59 ± 0.09	28.39 ± 0.08	⋯	⋯
F277DA J072252.57-732807.65	F277DA-045	>29.16	>29.54	>29.73	30.63 ± 0.34	29.43 ± 0.11	>30.72	⋯	⋯
F277DA J072233.84-732800.85	F277DA-046	>29.16	>29.54	>29.73	>30.66	29.33 ± 0.15	29.60 ± 0.19	⋯	⋯
F277DA J072237.79-732758.63	F277DA-047	>29.16	>29.54	>29.73	29.70 ± 0.22	28.77 ± 0.09	29.44 ± 0.16	⋯	⋯
F277DA J072242.11-732754.78	F277DA-049	>29.16	>29.54	>29.73	>30.66	29.57 ± 0.13	>30.72	⋯	⋯

(This table is available in machine-readable form.)

The Le Phare SED fitting results of our objects are detailed in Appendix C, and the key statistics are summarized in Figure A1. The statistics of T, M, and SFR are done on the subsets that retain only the objects that either the primary or the secondary solutions have $z_{\rm ph} \geqslant 11$ (rounded off to integers). If the primary solution has $z_{\rm ph} \geqslant 11$, these parameters are

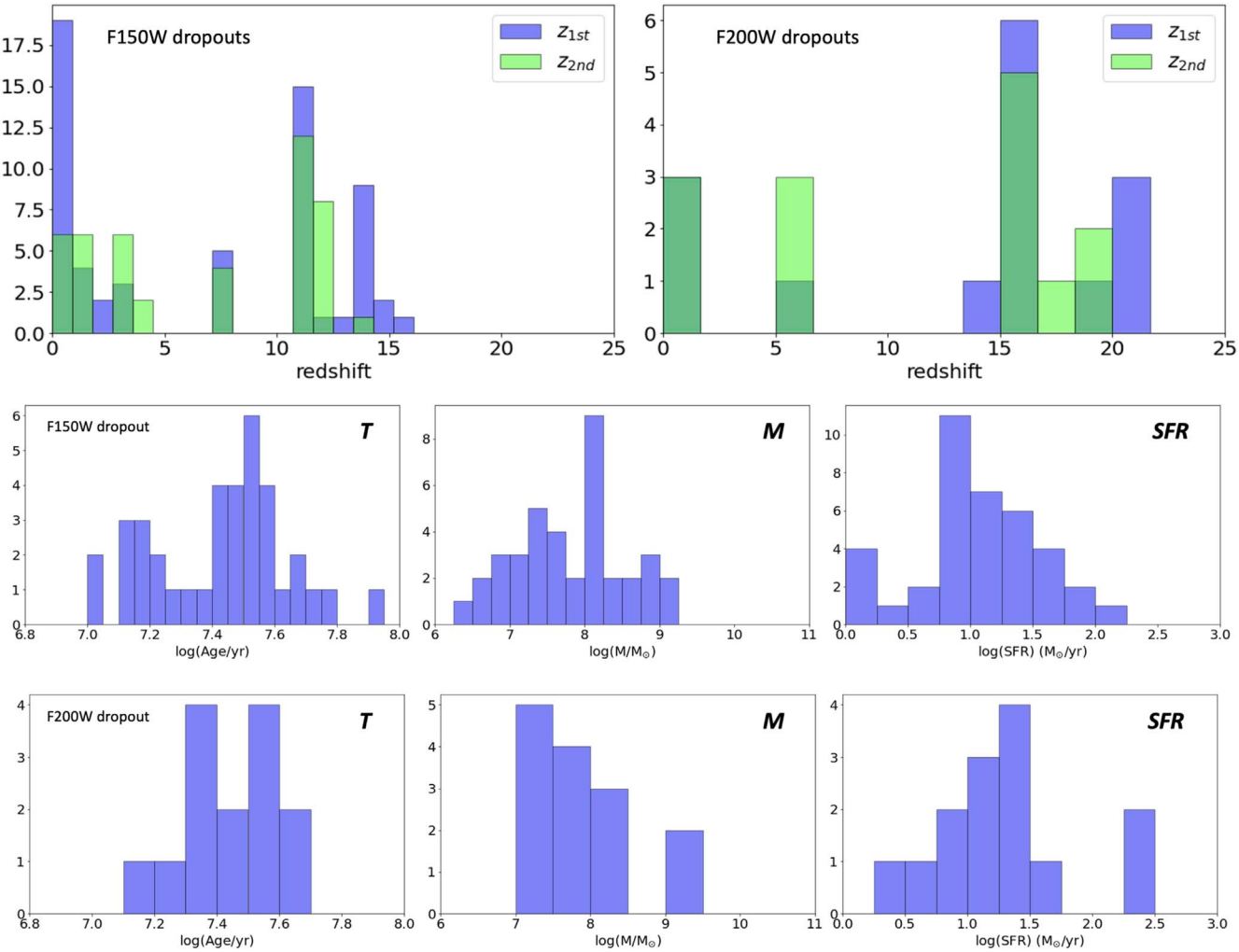

Figure A1. Summary of physical properties of F150W and F200W dropouts as derived by the Le Phare SED analysis. The top panel shows the distribution of z_{ph}. The best-fit z_{ph}, which correspond to the first peaks in the PDFs, are shown in blue. If the secondary peaks exist in the PDFs, the corresponding z_{ph} are shown in green. The middle and bottom panels show the distributions of age (T), stellar mass (M), and star formation rate (SFR) of the best-fit models corresponding to the first PDF peaks. The latter two statistics have taken into account the amplification due to lensing in module B. Stellar masses of the $z < 11$ interlopers are not included in the middle plot.

calculated at this solution; if only the secondary solution has $z_{ph} \geqslant 11$, these parameters are calculated at the secondary solution. In total, the subset contains 39 (14) F150W (F200W) dropouts.

The details of the EAZY SED fitting for z_{ph} are presented in Appendix D. Based on the z_{ph} estimates from these two different methods, we further group the F150W and F200W dropouts into four categories (indicated by "G_{ph}" in Table 1) based on whether their z_{ph} are at high-z (>11.0 for the F150W dropouts and >15.0 for the F200W dropouts, respectively): (i) both methods have the primary solution (corresponding to the primary peak of $P(z)$) at high-z; (ii) either method has the primary solution at high-z; (iii) neither method has the primary solution at high-z but at least one has the secondary solution (corresponding to the secondary peak of $P(z)$) at high-z; (iv) neither method has the primary nor the secondary solution at high-z. While such a grouping is not necessarily a ranking of the quality of these dropouts, it could be useful for follow-up studies in the future.

Three days after our Letter was submitted to arXiv, Atek et al. (2022) and Donnan et al. (2022) also submitted their papers to arXiv and they discussed high-z objects in SMACS 0723-73 as well. Among the nine $z \approx 11$–16 candidates in Atek et al. (2022), their SMACS_z11b, SMACS_z12b, and SMACS_z11e correspond to our F150DA-63, F150DA-77, and F150DA-81, respectively. Their SMACS_z16a and SMACS_z16b were selected by us as initial F200W dropouts but were rejected in the visual inspection step because they are visible in the veto band (F150W). Their SMACS_z11a, SMACS_z11c, SMACS_z11d, and SMACS_z12a do not meet our F150W dropout selection criteria either because of the less prominent color decrement or due to not having S/N $\geqslant 5$ in F200W. Donnan et al. (2022) also included nine $z \approx 11$–16 candidates, but only four of them are in SMACS 0723-73. Their ID 6486 does not meet our F150W dropout color criterion. Their 21901, 35470, 40079 were selected by us as initial F150W dropouts in module B but were later rejected because they all have $m_{200} > 28.70$ and are fainter than the depth threshold that we set for F150W dropout selection in module B.

Upon finishing this Letter, we came to be aware of a possible NIRCam flux calibration adjustment, which would require rescaling of the current pipeline reduced products. In the six bands relevant here, the scaling factors are 1.143, 1.028, 1.091, 0.870, 0.860, 0.815, from the bluest to the reddest, respectively. These correspond to adding the following numbers to the magnitudes derived using the original zero-point: −0.145,

−0.030, −0.095, 0.151, 0.164, and 0.222, from the bluest to the reddest, respectively. As none of these scaling factors have been vetted and any of them could be evolving in the next few months, we chose not to make these changes to our photometry.

Nonetheless, we still investigate how such changes could impact our dropout samples. As it turns out, all our F150W dropouts would still survive, and the new $z_{\rm ph}$ statistics would not change. Five of the F200W dropouts would have $m_{200} - m_{277} < 0.8$ mag (ranging from 0.65 to 0.78 mag); however, the new z_{ph} estimates would still put them at high-z. This is understandable because this is equivalent to lowering the color decrement threshold from 0.8 to 0.65 mag, or in other words, the Lyman-break signature moves 45% instead of 50% out of the dropout band. Therefore, none of our conclusions would be changed.

Appendix B
Dropout Images

Figures B1, B2, and B3 present the image cutouts of all our F150W, F200W, and F277W dropouts, respectively. The "chain of five" is already presented in Figure 3 and is not included here.

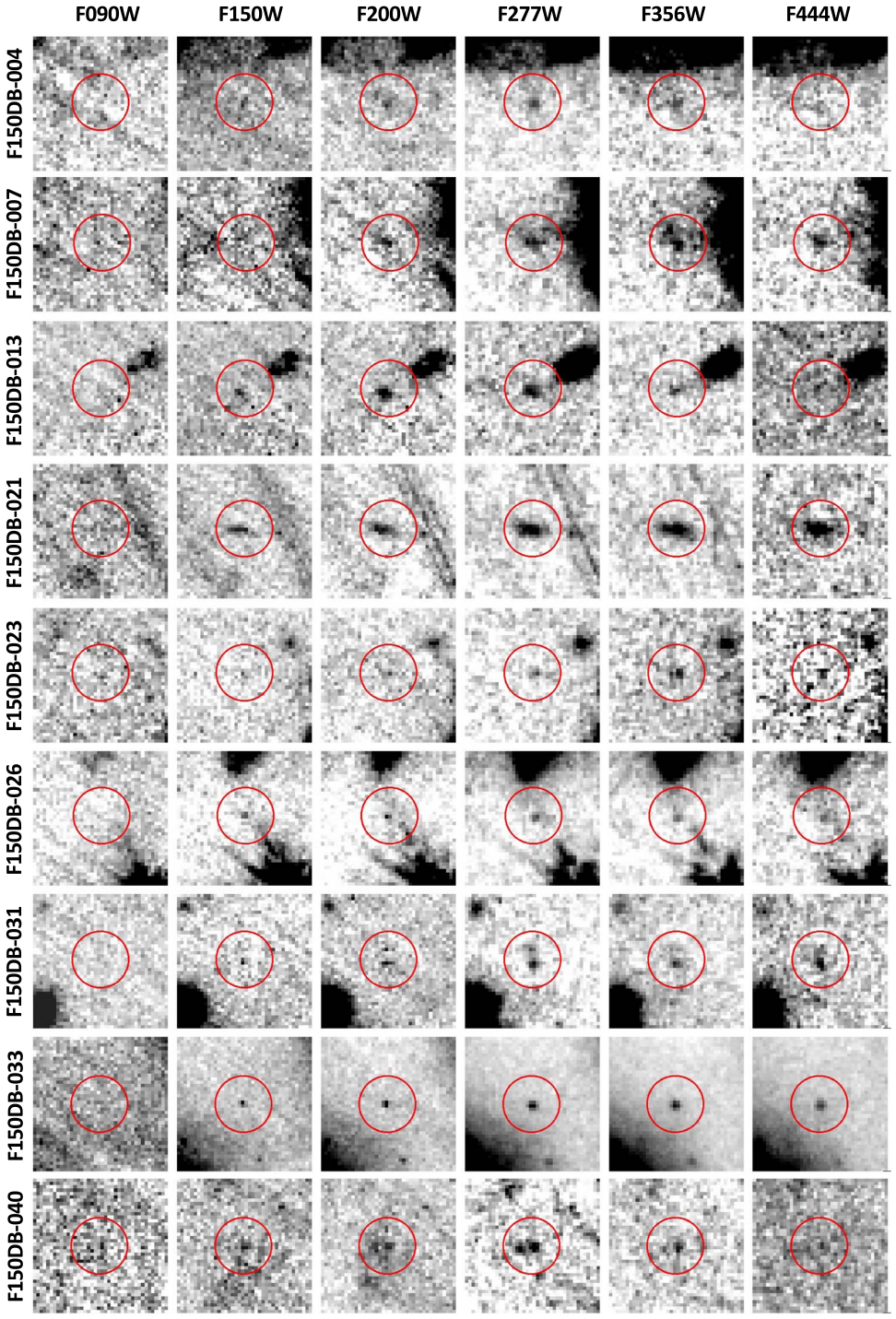

Figure B1. Image cutouts of F150W dropouts in fixed NIRCam bands. The images are $2\farcs4 \times 2\farcs4$ in size, and the dropout positions are indicated by the red circles ($0\farcs5$ in radius). The dropout SIDs are labeled to left. (An extended version of this figure is available.)

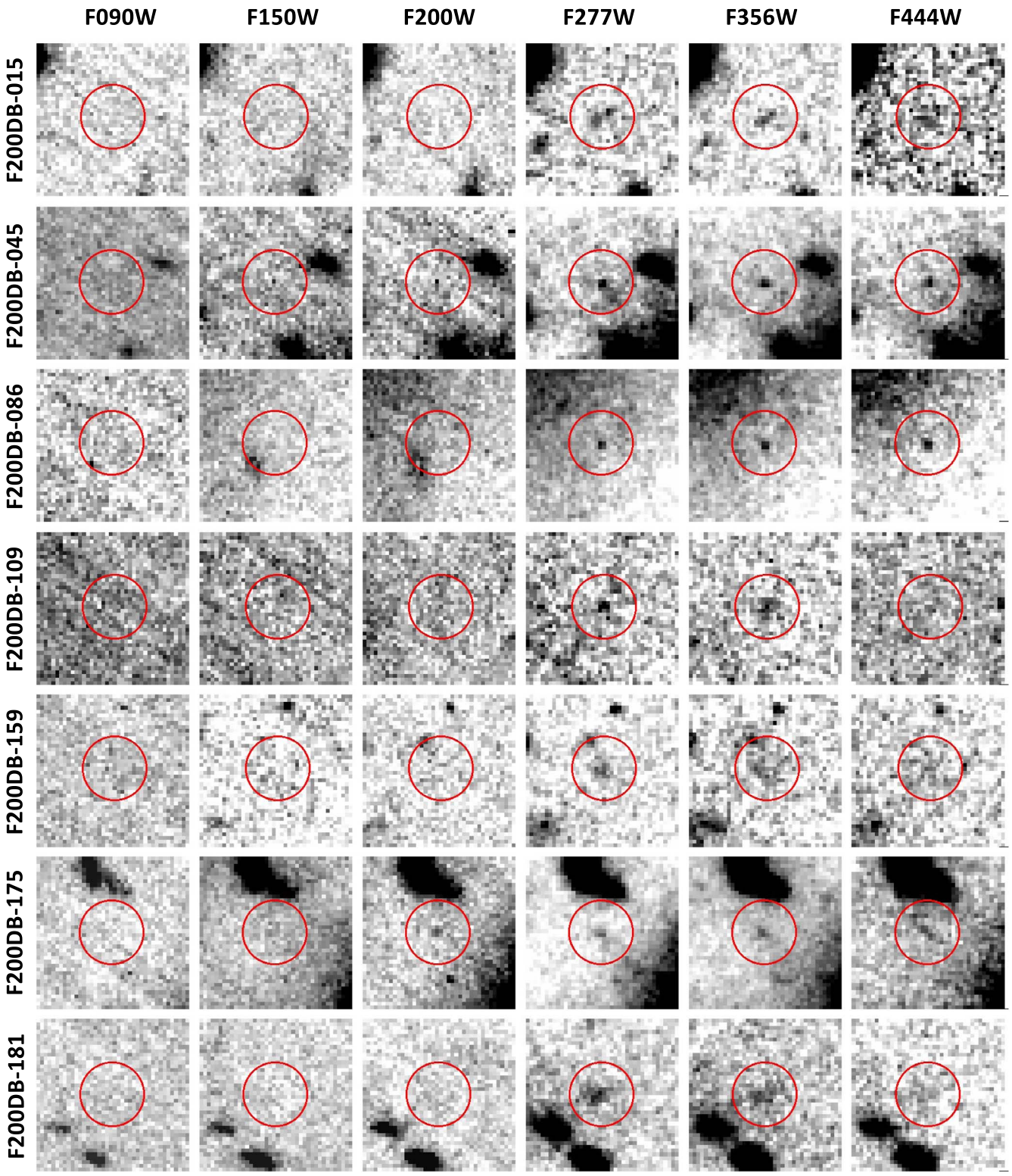

Figure B2. Similar to Figure B1, but for F200W dropouts. (An extended version of this figure is available.)

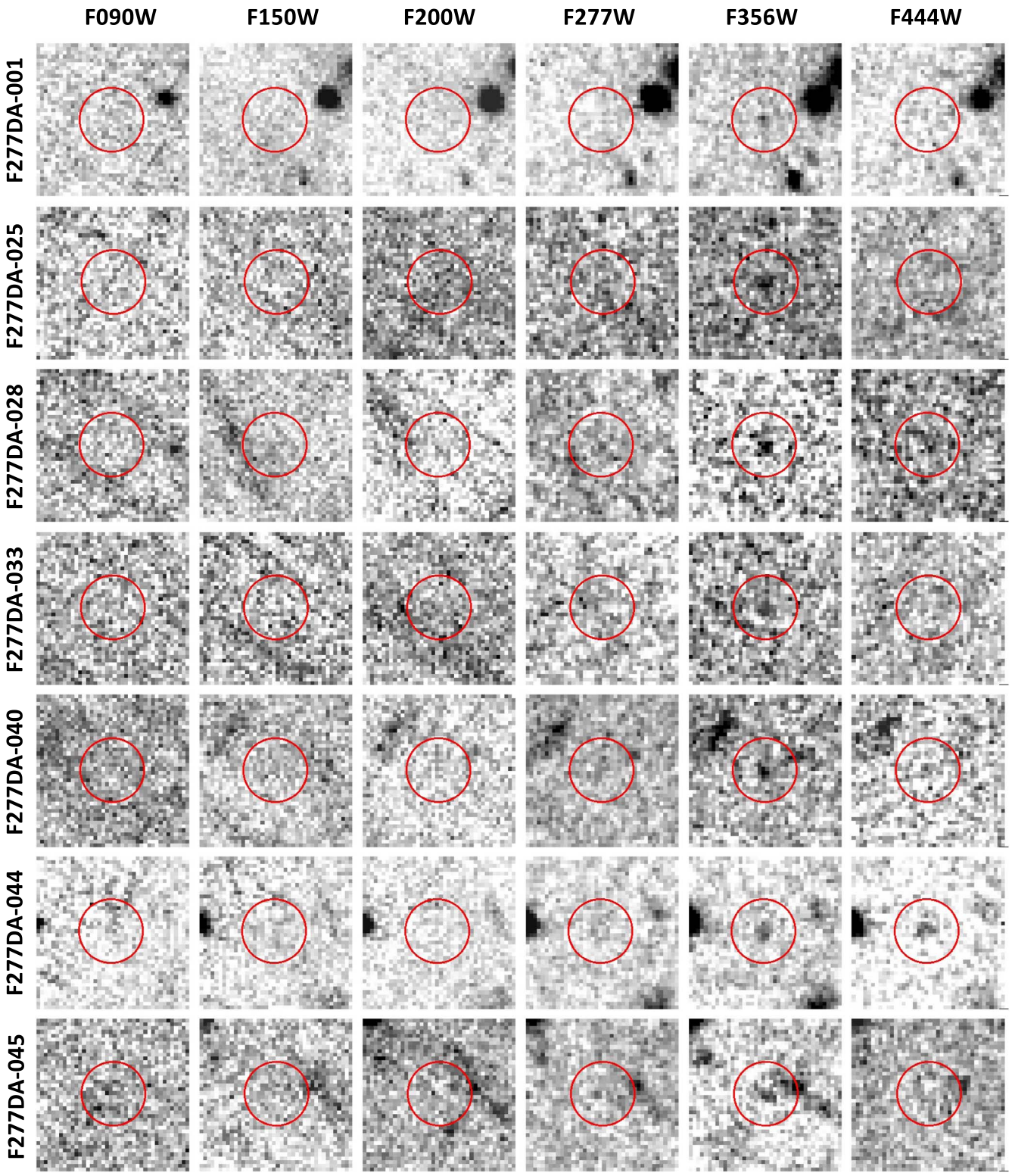

Figure B3. Similar to Figure B1, but for F277W dropouts.

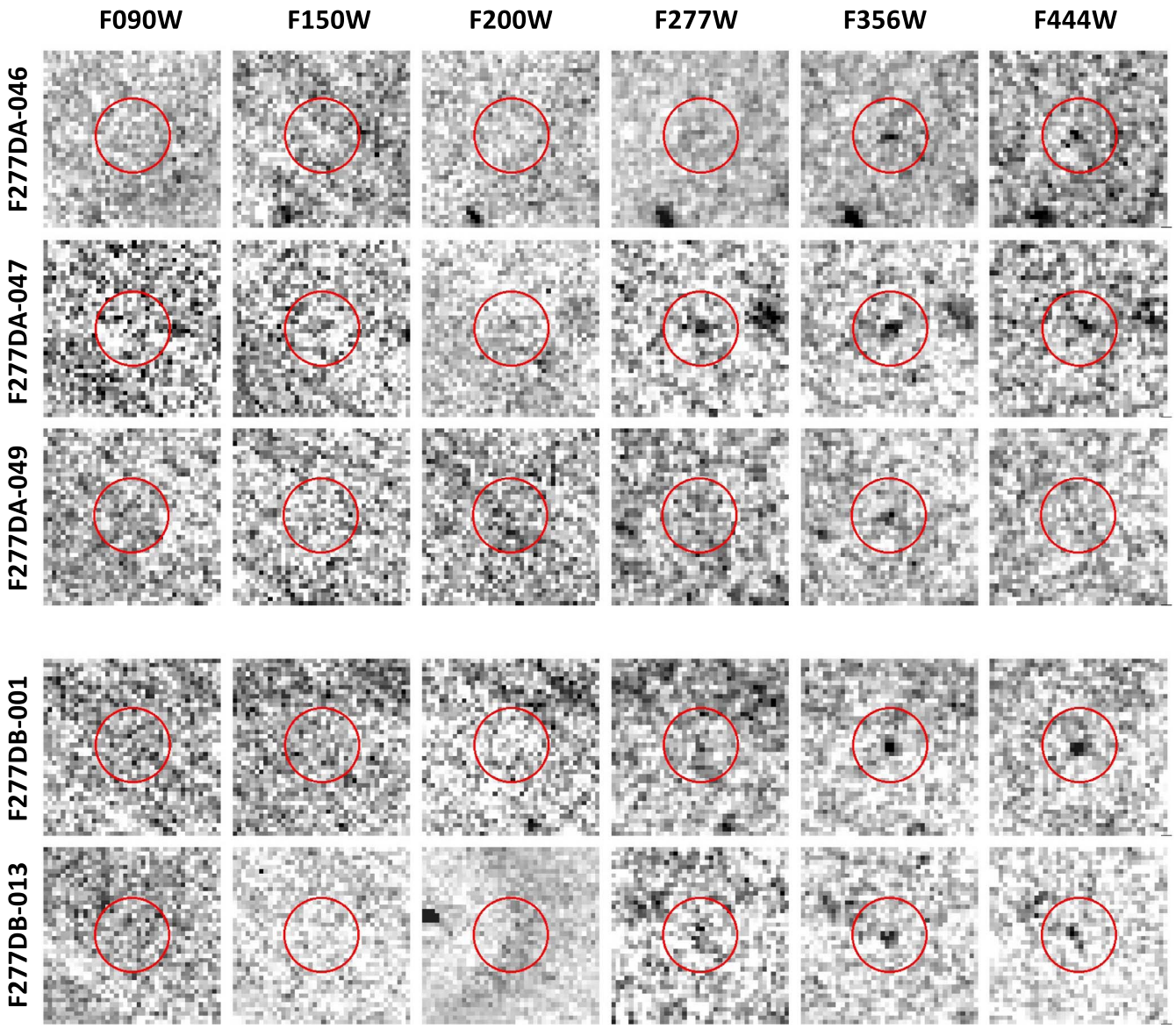

Figure B3. (Continued.)

Appendix C
Le Phare SED Fitting

Figure C1 and C2 present the SED fitting results for the F150W and F200W dropouts, using Le Phare and BC03 models as described in Section 4.2. These are similar to those shown in Figures 2 and 4. The "chain of five" are not included, as their photometry is severely affected by blending. The quoted χ^2 are the total values (i.e., not the "reduced χ^2").

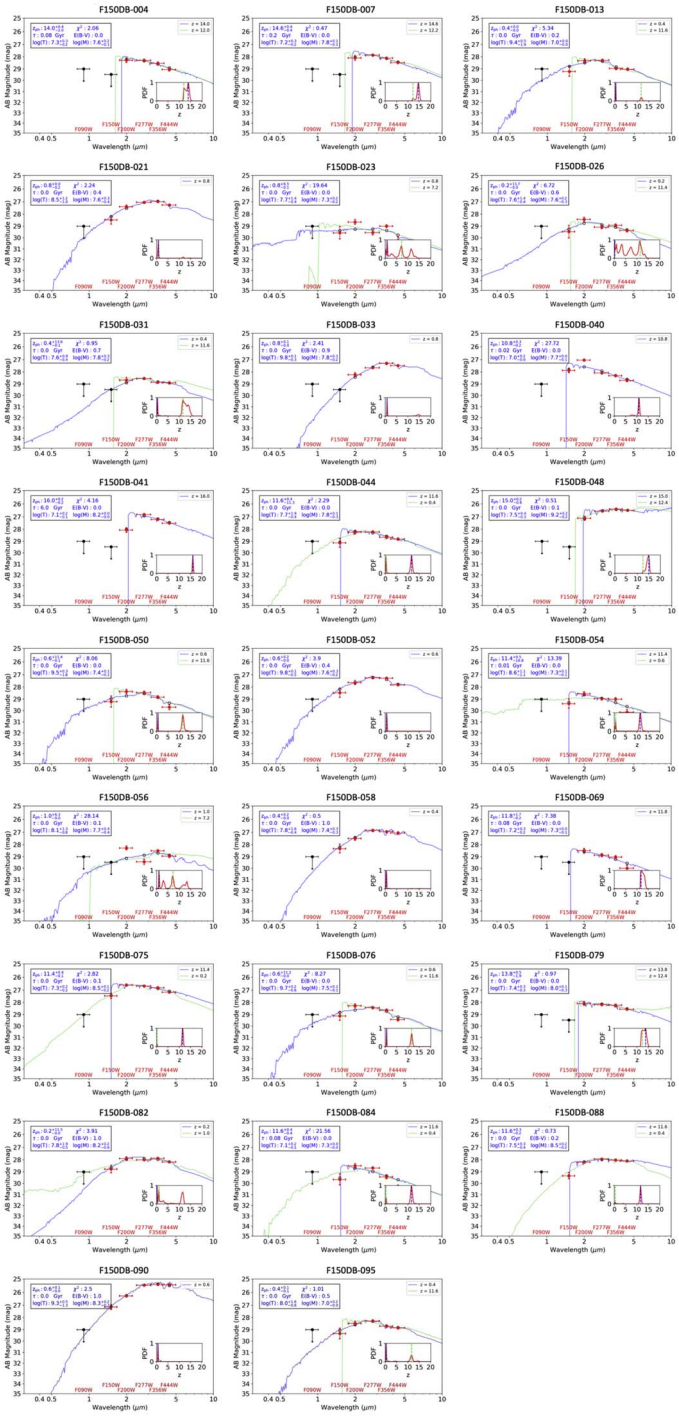

Figure C1. Le Phare SED fitting for F150W dropouts.

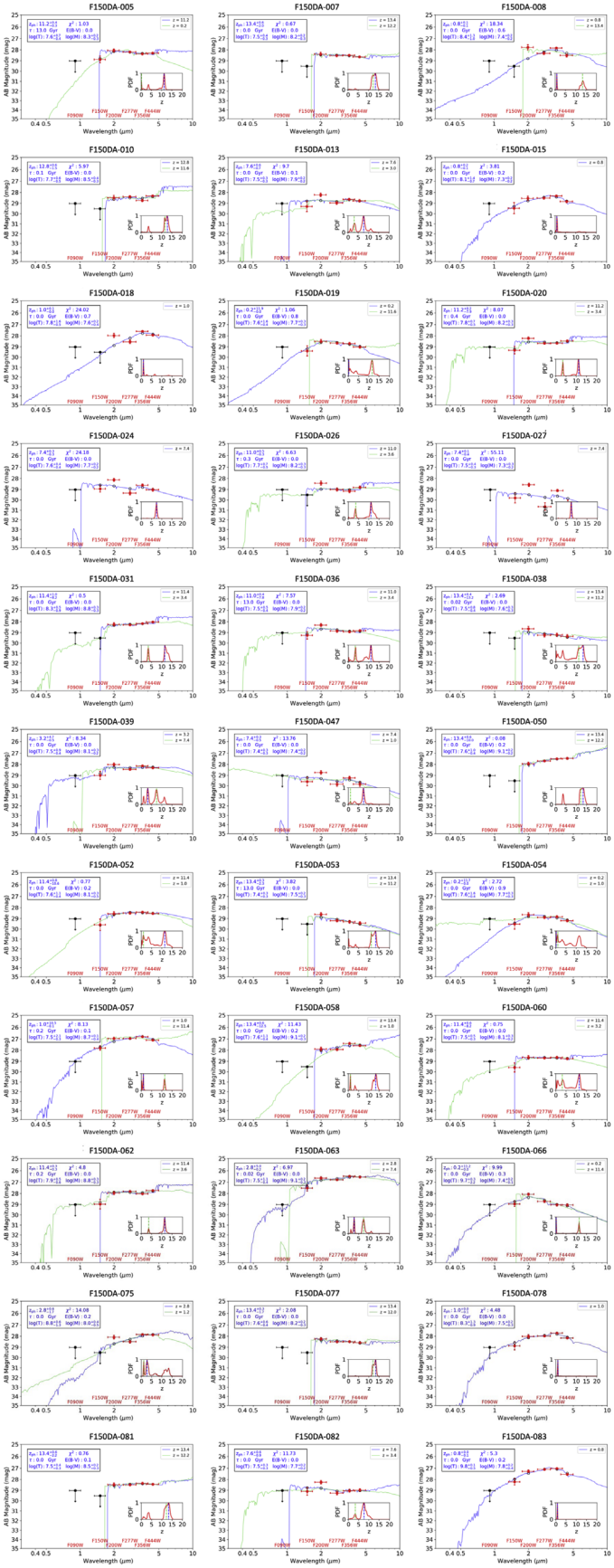

Figure C1. (Continued.)

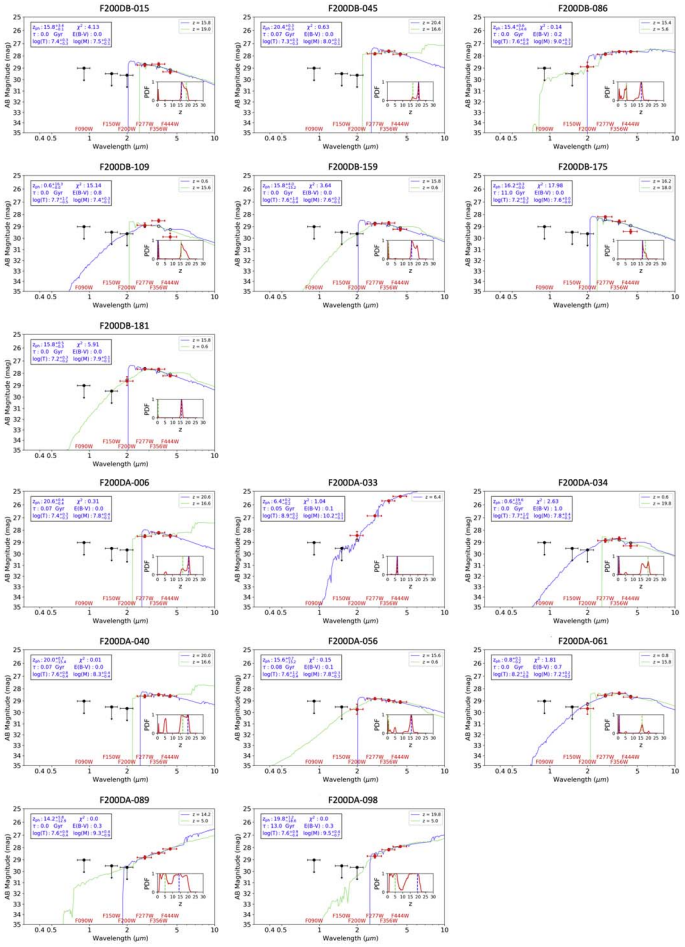

Figure C2. Le Phare SED fitting for F200W dropouts.

Appendix D
EAZY SED Fitting

We also performed SED fitting using EAZY-py[10], the latest implementation of EAZY, which incorporates templates with emission lines. Figures D1 and D2 show the results. We made a modification to the code so that flux density upper limits can be used. By design, EAZY is for $z_{\rm ph}$ derivation but is not for stellar population analysis. The black boxes with error bars are the data points, and the black curves are the best-fit models. The red circles are the synthesized flux densities based on the best-fit models. $P(z)$ is shown next to the SED plot in each panel. The quoted χ^2 are the total values.

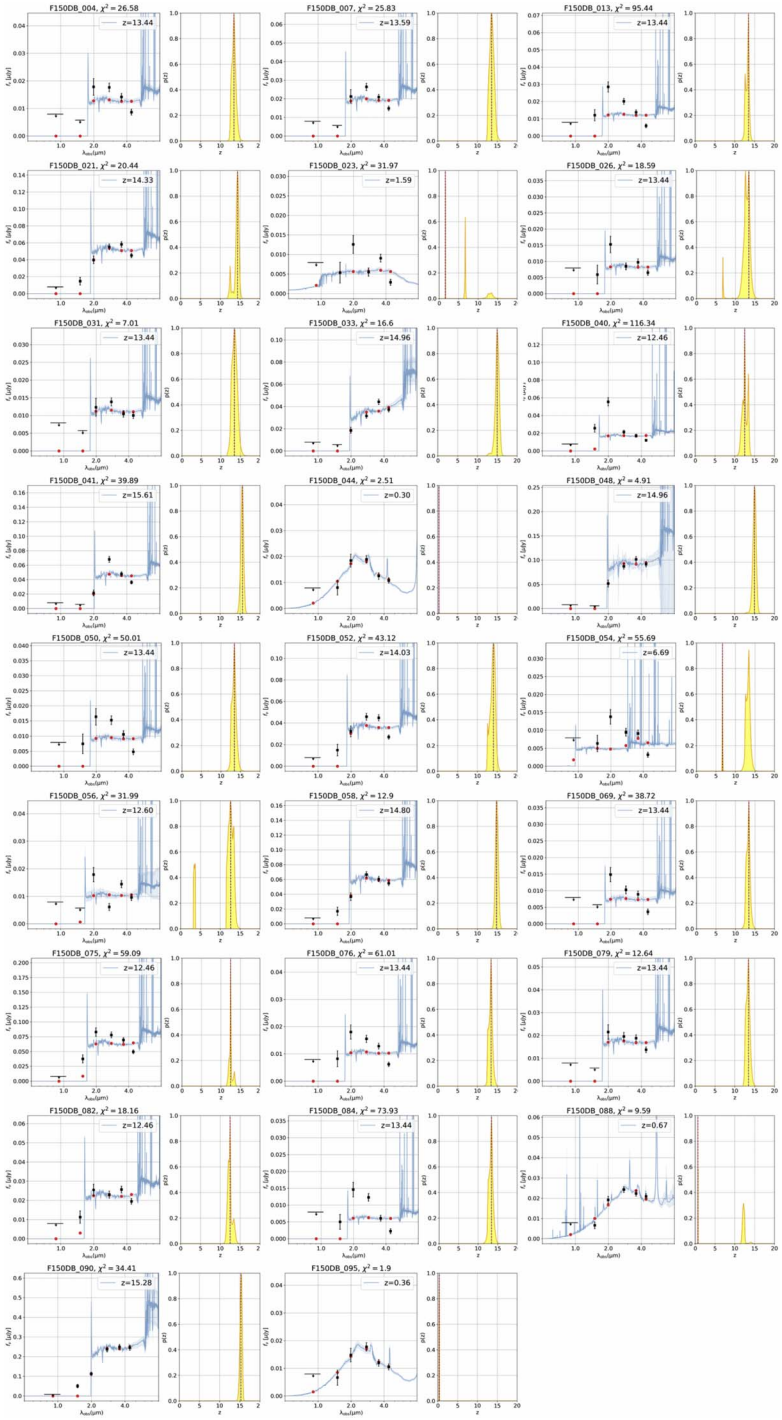

Figure D1. EAZY SED fitting for F150W dropouts.

[10] https://github.com/gbrammer/eazy-py

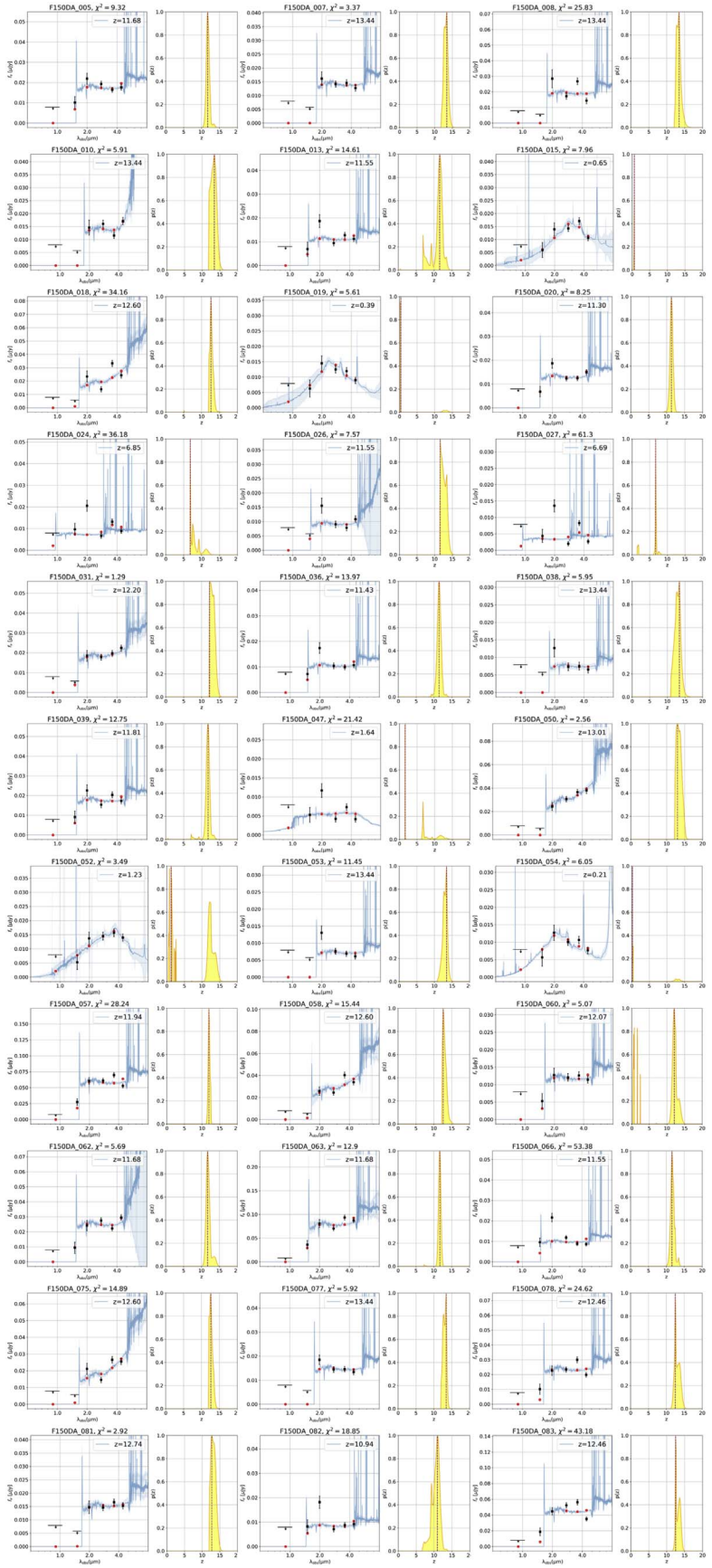

Figure D1. (Continued.)

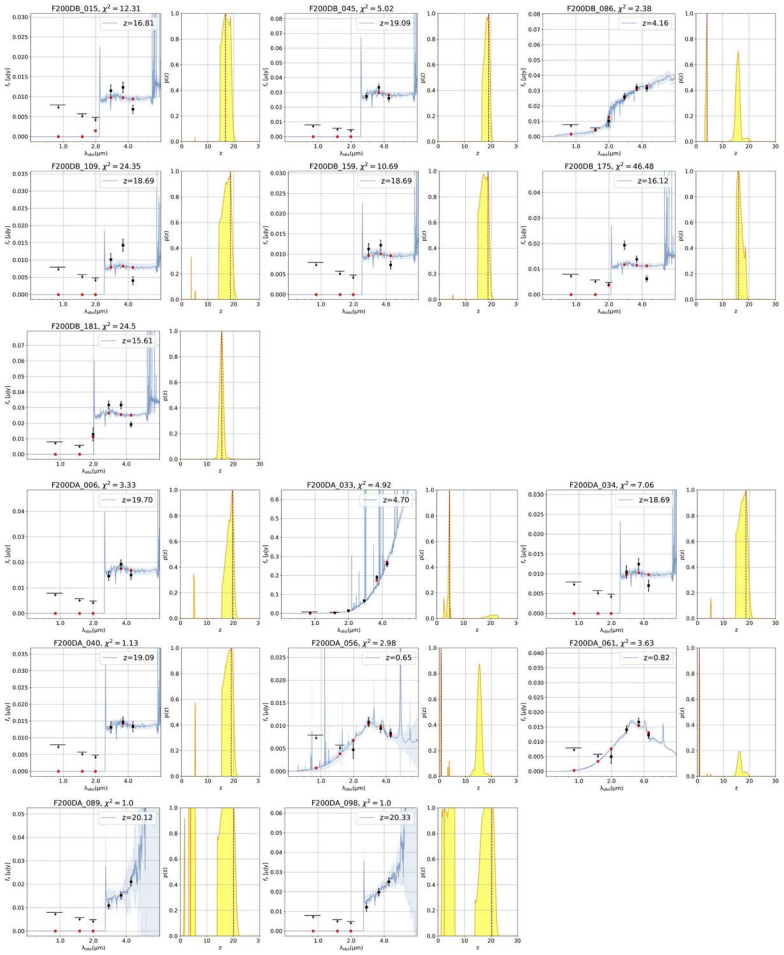

Figure D2. EAZY SED fitting for F200W dropouts.

ORCID iDs

Haojing Yan https://orcid.org/0000-0001-7592-7714
Zhiyuan Ma https://orcid.org/0000-0003-3270-6844
Chenxiaoji Ling https://orcid.org/0000-0003-4952-3008
Cheng Cheng https://orcid.org/0000-0003-0202-0534
Jia-Sheng Huang https://orcid.org/0000-0001-6511-8745

References

Arnouts, S., Cristiani, S., Moscardini, L., et al. 1999, MNRAS, 310, 540
Atek, H., Kneib, J.-P., Pacifici, C., et al. 2014, ApJ, 789, 96
Atek, H., Shuntov, M., Furtak, L. J., et al. 2022, arXiv:2207.12338
Atek, H., Siana, B., Scarlata, C., et al. 2011, ApJ, 743, 121
Behroozi, P., Conroy, C., Wechsler, R. H., et al. 2020, MNRAS, 499, 5702
Bertin, E., & Arnouts, S. 1996, A&AS, 117, 393
Bouwens, R. J., Illingworth, G. D., Oesch, P. A., et al. 2015, ApJ, 803, 34
Bouwens, R. J., Illingworth, G. D., Thompson, R. I., et al. 2004, ApJL, 606, L25
Bowman, J. D., Rogers, A. E. E., Monsalve, R. A., Mozdzen, T. J., & Mahesh, N. 2018, Natur, 555, 67
Bradley, L. D., Zitrin, A., Coe, D., et al. 2014, ApJ, 792, 76
Brammer, G. B., van Dokkum, P. G., & Coppi, P. 2008, ApJ, 686, 1503
Bruzual, G., & Charlot, S. 2003, MNRAS, 344, 1000
Burrows, A., Sudarsky, D., & Hubeny, I. 2006, ApJ, 640, 1063
Calzetti, D. 2001, PASP, 113, 1449
Caminha, G. B., Suyu, S. H., Mercurio, A., et al. 2022, arXiv:2207.07567
Cardamone, C., Schawinski, K., Sarzi, M., et al. 2009, MNRAS, 399, 1191
Castellano, M., Fontana, A., Treu, T., et al. 2022, arXiv:2207.09436
Chabrier, G. 2003, PASP, 115, 763
Chary, R.-R., Stern, D., & Eisenhardt, P. 2005, ApJL, 635, L5
Cheng, C., Yan, H., Huang, J.-S., et al. 2022, ApJL, 936, L19
Coe, D., Salmon, B., Bradač, M., et al. 2019, ApJ, 884, 85
Coe, D., Zitrin, A., Carrasco, M., et al. 2013, ApJ, 762, 32
Donnan, C. T., McLeod, D. J., Dunlop, J. S., et al. 2022, arXiv:2207.12356
Fan, X., Carilli, C. L., & Keating, B. 2006, ARA&A, 44, 415
Finkelstein, S. L., Bagley, M. B., Arrabal Haro, P., et al. 2022, arXiv:2207.12474
Finkelstein, S. L., Papovich, C., Salmon, B., et al. 2012, ApJ, 756, 164
Golubchik, M., Furtak, L. J., Meena, A. K., & Zitrin, A. 2022, arXiv:2207.05007
Hashimoto, T., Laporte, N., Mawatari, K., et al. 2018, Natur, 557, 392
Ilbert, O., Arnouts, S., McCracken, H. J., et al. 2006, A&A, 457, 841
Ishigaki, M., Kawamata, R., Ouchi, M., et al. 2018, ApJ, 854, 73
Jiang, L., Kashikawa, N., Wang, S., et al. 2021, NatAs, 5, 256
Mahler, G., Jauzac, M., Richard, J., et al. 2022, arXiv:2207.07101
Malkan, M. A., Cohen, D. P., Maruyama, M., et al. 2017, ApJ, 850, 5
McLeod, D. J., McLure, R. J., & Dunlop, J. S. 2016, MNRAS, 459, 3812
McLure, R. J., Dunlop, J. S., Bowler, R. A. A., et al. 2013, MNRAS, 432, 2696
Naidu, R. P., Oesch, P. A., van Dokkum, P., et al. 2022, arXiv:2207.09434
Oesch, P. A., Bouwens, R. J., Illingworth, G. D., et al. 2012a, ApJ, 745, 110
Oesch, P. A., Bouwens, R. J., Illingworth, G. D., et al. 2012b, ApJ, 759, 135
Oesch, P. A., Bouwens, R. J., Illingworth, G. D., Labbé, I., & Stefanon, M. 2018, ApJ, 855, 105
Pascale, M., Frye, B., Diego, J., et al. 2022, arXiv:2207.07102
Planck Collaboration, Adam, R, Aghanim, N., et al. 2016, A&A, 596, A108
Pontoppidan, K., Blome, C., Braun, H., et al. 2022, arXiv:2207.13067
Roberts-Borsani, G. W., Ellis, R. S., & Laporte, N. 2020, MNRAS, 497, 3440
Stanway, E. R., Bunker, A. J., McMahon, R. G., et al. 2004, ApJ, 607, 704
Steidel, C. C., Pettini, M., & Hamilton, D. 1995, AJ, 110, 2519
Sun, F., Egami, E., Pérez-González, P. G., et al. 2021, ApJ, 922, 114
Vogelsberger, M., Nelson, D., Pillepich, A., et al. 2020, MNRAS, 492, 5167
Yan, H., Finkelstein, S. L., Huang, K.-H., et al. 2012, ApJ, 761, 177
Yan, H., & Windhorst, R. A. 2004, ApJL, 612, L93
Yan, H.-J., Windhorst, R. A., Hathi, N. P., et al. 2010, RAA, 10, 867
Zavala, J. A., Buat, V., Casey, C. M., et al. 2022, arXiv:2208.01816
Zheng, W., Postman, M., Zitrin, A., et al. 2012, Natur, 489, 406
Zitrin, A., Broadhurst, T., Umetsu, K., et al. 2009, MNRAS, 396, 1985